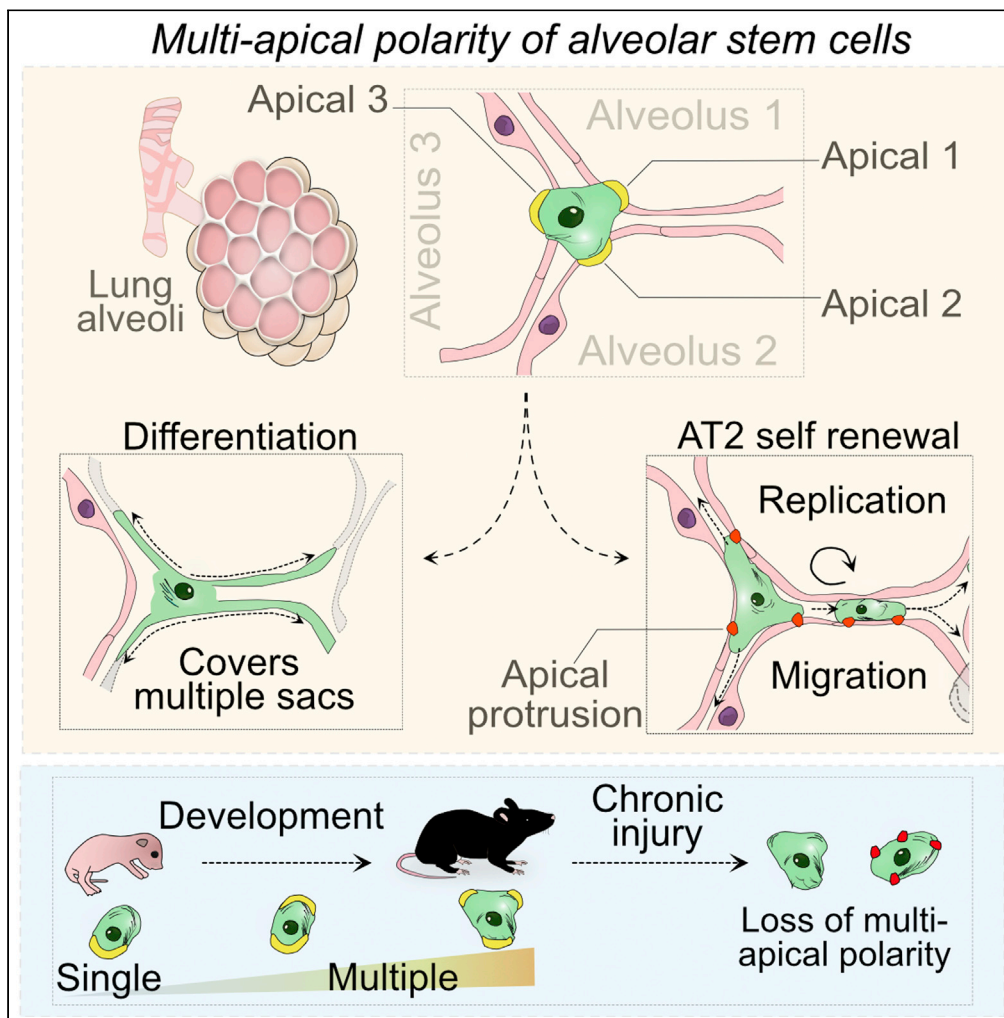## Article

# Multi-apical polarity of alveolar stem cells and their dynamics during lung development and regeneration

Arvind Konkimalla,
Satoshi Konishi,
Yoshihiko
Kobayashi, ...,
Jose Javier Bravo-
Cordero,
Aleksandra Tata,
Purushothama
Rao Tata

aleksandra.tata@duke.edu
(A.T.)
purushothamarao.tata@duke.
edu (P.R.T.)

### Highlights

Alveolar stem cells show
unique multi-apical
polarity and en face
multiple lumens

Multi-apical polarity is
gradually established
during postnatal lung
development

AT2s reestablish multi-
apical polarity during
injury repair

Chronic lung injury and
oncogene activation
disrupts multi-apical
polarity

## Article

# Multi-apical polarity of alveolar stem cells and their dynamics during lung development and regeneration

Arvind Konkimalla,[1,2] Satoshi Konishi,[1] Yoshihiko Kobayashi,[1,13] Preetish Kadur Lakshminarasimha Murthy,[1,14] Lauren Macadlo,[1] Ananya Mukherjee,[3] Zachary Elmore,[4] So-Jin Kim,[5] Ann Marie Pendergast,[6,7] Patty J. Lee,[5] Aravind Asokan,[4,8,9,10] Lars Knudsen,[11] Jose Javier Bravo-Cordero,[3] Aleksandra Tata,[1,*] and Purushothama Rao Tata[1,5,7,10,12,15,*]

## SUMMARY

**Epithelial cells of diverse tissues are characterized by the presence of a single apical domain. In the lung, electron microscopy studies have suggested that alveolar type-2 epithelial cells (AT2s) en face multiple alveolar sacs. However, apical and basolateral organization of the AT2s and their establishment during development and remodeling after injury repair remain unknown. Thick tissue imaging and electron microscopy revealed that a single AT2 can have multiple apical domains that enface multiple alveoli. AT2s gradually establish multi-apical domains post-natally, and they are maintained throughout life. Lineage tracing, live imaging, and selective cell ablation revealed that AT2s dynamically reorganize multi-apical domains during injury repair. Single-cell transcriptome signatures of residual AT2s revealed changes in cytoskeleton and cell migration. Significantly, cigarette smoke and oncogene activation lead to dysregulation of multi-apical domains. We propose that the multi-apical domains of AT2s enable them to be poised to support the regeneration of a large array of alveolar sacs.**

## INTRODUCTION

Epithelial tissue homeostasis requires a precise, dynamic balance between the gain and loss of cells within geometrically defined boundaries (Blanpain and Fuchs, 2014; Clevers et al., 2014; Clevers and Watt, 2018; Fuchs and Blau, 2020; Fuchs and Steller, 2015; Lay et al., 2018; Rompolas et al., 2013, 2016; Xin et al., 2016). In most adult epithelia, homeostasis is maintained by resident stem cells, which can migrate to damaged regions to proliferate and differentiate into other functional cell types (Blanpain and Fuchs, 2014; Clevers and Watt, 2018). Stem cell numbers and their distribution and spatial organization within defined niches, vary depending on tissue architecture and functional needs (Hsu et al., 2011; Pardo-Saganta et al., 2015; Rompolas et al., 2013; Tata et al., 2013; Tata and Rajagopal, 2016; Xin et al., 2016). Mechanisms of repair and regeneration of damaged epithelia must also restore cellular characteristics such as cell shape, size, number, and architecture, including apical and basolateral polarity.

The distal region of the lung is made up of millions of air-filled, vascularized sacs lined by two epithelial cell types: alveolar type-1 (AT1) and alveolar type-2 (AT2) cells. AT1s are very thin, terminally differentiated and have a large surface area covering 95% of the alveolar luminal surface (Mercer et al., 1994; Weibel et al., 2005; Weibel and Gomez, 1962). Electron microscopy studies have suggested that a single AT1 cell can contribute structurally to multiple alveolar sacs (Weibel, 2015). AT2s are cuboidal, sparsely distributed among the AT1s, and makeup only 5% of the total surface area (Knust et al., 2009; Mercer et al., 1994; Schulte et al., 2019; Weibel et al., 2005). AT2s secrete surfactants and have the ability to self-renew and differentiate into AT1s thereby serving as stem cells of the alveolar epithelium (Barkauskas et al., 2013; Desai et al., 2014; Nabhan et al., 2018; Zacharias et al., 2018). Of interest, classical electron microscopy studies from the 1970s suggested that AT2s face multiple alveolar lumens (Cordingley, 1972; Weibel, 1971). Despite these observations, AT2s are generally depicted as located on the basal lamina with their cell bodies directly facing the lumen of a single alveolar sac (Hogan et al., 2014; Zepp and Morrisey, 2019).

[1]Department of Cell Biology, Duke University School of Medicine, Durham, NC 27710, USA

[2]Medical Scientist Training Program, Duke University School of Medicine, Durham, NC 27710, USA

[3]Division of Hematology and Oncology, Department of Medicine, Tisch Cancer Institute, Icahn School of Medicine at Mount Sinai, New York, NY 10029, USA

[4]Department of Surgery, Duke University School of Medicine, Durham, NC 27710, USA

[5]Division of Pulmonary, Allergy, and Critical Care Medicine, Department of Medicine, Duke University School of Medicine and the Durham Veterans Administration Medical Center, Durham, NC 27710, USA

[6]Department of Pharmacology and Cancer Biology, Duke University School of Medicine, Durham, NC 27710, USA

[7]Duke Cancer Institute, Duke University School of Medicine, Durham, NC 27710, USA

[8]Department of Molecular Genetics and Microbiology, Duke University School of Medicine, Durham, NC 27710, USA

[9]Department of Biomedical Engineering, Regeneration Next, Duke University, Durham, NC 27710, USA

[10]Center for Advanced Genomic Technologies, Duke University, Durham, NC 27710, USA

[11]Institute of Functional and Applied Anatomy, Hannover

*Continued*

Indeed, little attention has been paid to the actual cellular architecture of AT2 cells and their apical and basolateral polarity organization in the context of their multi-lumen enfacement.

Here, we have used thick tissue imaging to re-evaluate the organization of saccular alveolar tissue and the distribution of AT2s, their location, and structural organization. We find that AT2s have a unique cellular architecture with multiple apical polar domains that enable them to enface multiple alveolar saccules. Moreover, using lineage tracing, live imaging, and alveolar injury models, including bleomycin injury and selective AT2 or AT1 cell ablation, we describe the dynamic loss and re-establishment of multi-apical polarity. In addition, we used single-cell transcriptome profiling to assess molecular signatures associated with AT2s proliferation and migration. Finally, we implicate dysregulation of multi-apical polarity in respiratory diseases including cigarette smoke-induced injury and oncogenic events.

## RESULTS

### A single AT2 enfaces multiple alveolar sacs via its multi-apical domains

First, we sought to enumerate AT2s per alveolus in adult murine lungs. For this purpose, we performed immunostaining analysis using specific AT2 (SFTPC) and AT1 (AGER) cell markers, coupled with thick tissue imaging to visualize multiple cup-shaped alveolar sacs (Figures S1A and S1B). Three-dimensional visualization and surface rendering revealed varied numbers of AT2s in individual alveoli. Quantification of SFTPC-expressing cells showed that on average about 26, 52, and 17% of the alveolar sacs are occupied by one, two, or three AT2s, respectively. Only about 5% of the cups are occupied by either zero or four cells (Figure S1C). Similar analysis of aged mice (1 year old) revealed a significant change in the peak number of AT2s, which shifted from two in young adults to one in older mouse lungs (Figures S1B and S1C). Next, we sought to determine the distribution of AT2s in alveolar cups. Three-dimensional rendering of alveoli revealed that most AT2s have their cell bodies embedded in the interstitium, with only a small region of the cell facing the alveolar lumen (Figure 1A and Video S1). Quantification revealed that, on average, about 48, 42, or 10% of AT2s enface one, two, or three alveolar cup(s), respectively (Figure S1B). To further visualize AT2 localization, we performed transmission electron microscopy (TEM) on lung sections. Consistent with previous observations, we found that a single AT2 can enface multiple lumens. Significantly, the TEM images reveal that membranes facing the lumen have foldings that resemble microvilli, structure that are characteristic of apical domains in the other epithelial tissues (Figures 1C and S2B). AT2s enfacing multiple lumens were also observed in rat and human lungs (Figures S2A and S2B).

To determine the polarity of AT2s that enface multiple lumina, we performed immunostaining for MUC1, a known apically localized protein that is specifically present on AT2s in alveolar epithelium (Desai et al., 2014). We found that in adult lungs a single AT2 cell (Sftpc-tdt[+] NKX2-1[+]) can have between one to four MUC1 enriched domains, each facing the lumina of different alveoli (Figures 2A–2D and S2C and Video S2). Similar multi-apical domains were observed in human AT2s, suggesting that such organization is conserved across species (Figure S2D). Of interest, we found that MUC1 enriched apical domains vary in size and shape and can be categorized into two types – flat, disc-shaped macrodomains and small apical protrusions (Figures 2E and S2C). Irrespective of the domain size, every apical domain faces an alveolar lumen. These findings were further confirmed using known other apical polarity markers including EZRIN and EPS8 (Figures 2G and 2H) (Huang et al., 2003). Moreover, co-immunostaining for CDH1 (also known as E-cadherin) and MUC1 revealed that each apical domain is surrounded by a ring of focally enriched CDH1, indicating the presence of adherens junctions at these sites (Figure 2I). Taken together, we identify a unique cellular organization and multi-apical polarity of AT2s in the lungs (Figure 2J).

### AT2s gradually establish multiple apical domains during postnatal development

Developing lungs undergo significant changes in cellular composition and tissue organization (Basil et al., 2020; Branchfield et al., 2016; Cardoso and Lü, 2006; Cardoso and Whitsett, 2008; Herriges and Morrisey, 2014; Hogan et al., 2014; Nikolić et al., 2018; Warburton et al., 2000; Zepp et al., 2021). Specifically, alveoli undergo secondary septation, which increases their surface area and gas exchange capacity. This process is accompanied by significant re-distribution of alveolar cells between postnatal days 0 to 25 (Pozarska et al., 2017). To ascertain the developmental emergence of multi-apical domains during murine lung maturation, we analyzed lungs from postnatal day 0 to day 25 (Figure 3A). Immunostaining of alveolar tissue for LAMP3, SFTPC, MUC1, AGER, and NKX2-1 on alveolar tissue revealed that MUC1 expression is specific to AT2s throughout all stages tested (Figures 3B and 3C). Before postnatal day 5 (PN5), AT2s predominantly contain a single MUC1 enriched apical domain. However, we observed the emergence of two and three

Medical School, Hannover 30625, Germany

[12]Duke Regeneration Center, Duke University, Durham, NC 27710, USA

[13]Current address: Institute for Frontier Life and Medical Sciences, Kyoto University, Kyoto, Japan

[14]Current address: Department of Pharmacology and Regenerative Medicine, University of Illinois at Chicago, Chicago, IL, 60612, USA

[15]Lead contact

*Correspondence:
aleksandra.tata@duke.edu (A.T.),
purushothamarao.tata@duke.edu (P.R.T.)
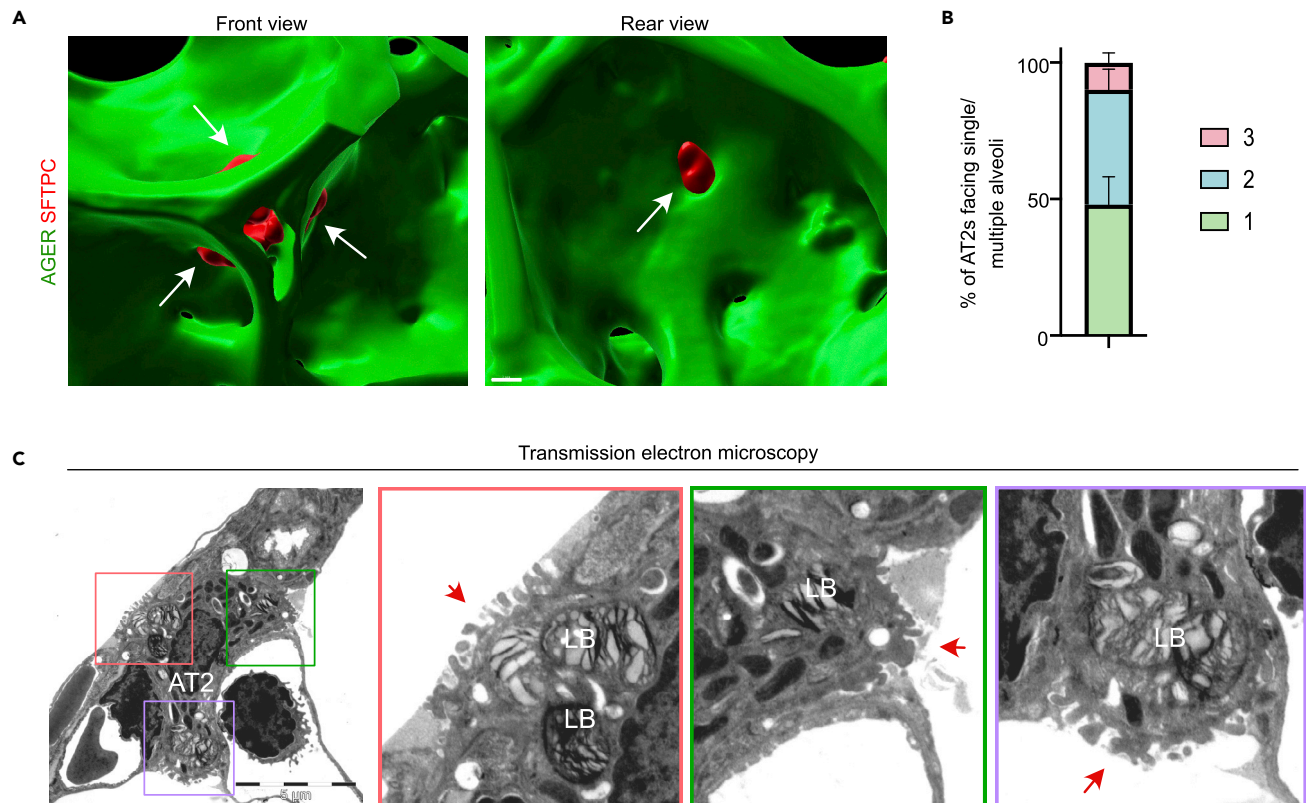https://doi.org/10.1016/j.isci.2022.105114

**Figure 1. A single AT2 enfaces multiple alveolar sacs**

(A) 3D rendering of alveolar sac (AGER, green) with single AT2 cell depicted in red. Front and rear views are shown. White arrows indicate multiple apically exposed surfaces of a single AT2 enfacing four adjacent alveolar cups. Scale bar: 3μm.

(B) Quantification of AT2s facing one (green column), two (blue column), or three (pink column) alveoli. n = 3 mice. Data are presented as mean ±SEM.

(C) Transmission electron micrograph of mouse AT2 cell facing three alveolar lumens. Color boxed inset indicates enlarged image on the right. Red arrows indicate AT2 cell facing lumen. LB- lamellar bodies. Scale bar: 5 μm. See also Figures S1, S2 and Video S1.

apical domains and a significant increase in their numbers between PN5 and PN25, by which time the number of MUC1 localized apical domains approximates those seen in adult lungs (Figure 3D). These data support a model in which AT2s gradually progress from uni-to multi-apical domains during postnatal stages as the alveoli increase in complexity (Figures 3A–3D).

## A single AT2 clonally propagates to both replenish cells and reestablish their localization in multiple alveolar sacs after repeated loss

Previous studies have demonstrated that AT2s can replicate and repair damaged epithelium in different injury models (Barkauskas et al., 2013; Choi et al., 2020; Hogan et al., 2014; Kobayashi et al., 2020; Lee et al., 2014; Nabhan et al., 2018; Strunz et al., 2020; Zacharias et al., 2018). We sought to test whether AT2s can recover their numbers and unique localization pattern (i.e., enface multiple alveolar sacs) following recurrent injuries. For this, we employed a *Sftpc-CreER;R26R-DTA;R26R-tdTomato* mouse line (in short, *Sftpc-DTA/tdT*), in which tamoxifen administration allows for selective ablation of AT2s and simultaneous lineage labeling (tdTomato) to track residual AT2 cell contribution during regeneration (Barkauskas et al., 2013). To assess the ability of AT2s to recover after recurrent injuries, we performed repeated ablation by administering tamoxifen in three successive rounds, each at 3-week intervals (Figure 4A). Consistent with previous findings, on day 3 after a single round of ablation we observed large swatches of alveoli devoid of AT2s, as revealed by immunostaining for SFTPC and confirmed by fluorescence-activated cell sorting (Figures 4B and 4C), suggesting efficient ablation. This coincided with a significant increase in AT2 replication as assessed by immunostaining for Ki67, a marker for cell proliferation (Figures S3A and S3B). Lungs collected at 3 weeks after each round (single, double, and triple) of ablation showed a significant recovery of AT2s. Quantification further revealed that about 60% of AT2s recover by
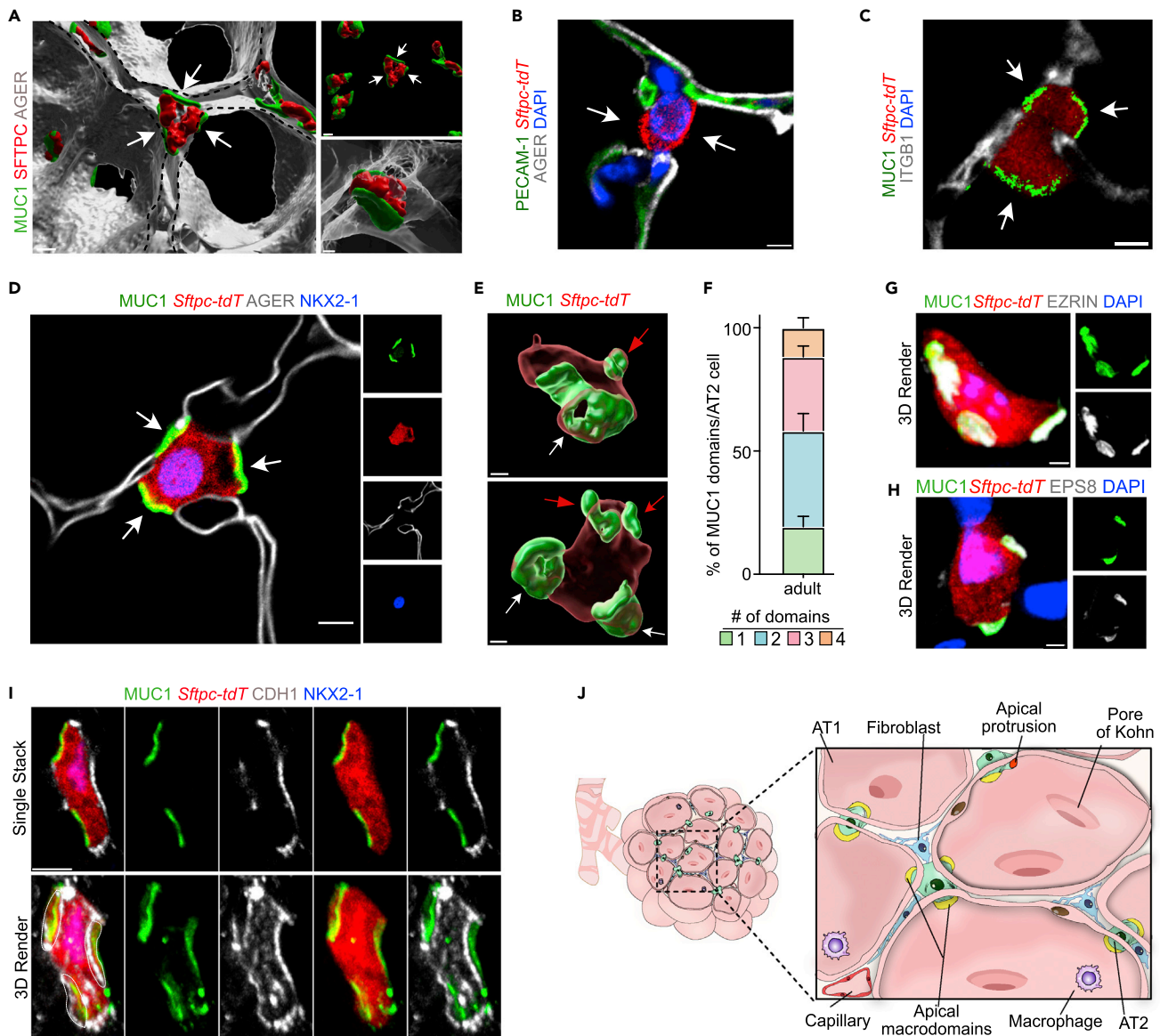
**Figure 2. AT2 cells contain multiple apical domains**

(A) 3D reconstruction of MUC1 domains (green), AT2 (red) and AT1 (gray) cells. Scale bar: 5 μm. A side view of AT2 cell with MUC1 domains is shown in right panel (bottom image, scale bar: 3 μm). White arrows indicate MUC1/alveolar enfacement.

(B) Immunostaining of wild-type mouse AT2s (red), PECAM-1 (green), and AGER (gray). White arrows indicate multiple apically exposed surfaces. DAPI stains nuclei. Scale bar: 4μm.

(C) Immunostaining of AT2 (red), MUC1 (green), and ITGB1 (gray). White arrows indicate multiple apically exposed surfaces. DAPI stains nuclei. Scale bar: 5μm.

(D) Immunostaining of AT2 (red), MUC1 (green), AGER (gray) and NKX2-1 (blue). White arrows indicate multiple apically exposed surfaces. Scale bar, 5μm.

(E) 3D reconstruction of lineage labeled AT2 cells (red) and their respective MUC1 domains (green). White arrows indicate apical macrodomains; red arrows indicate apical protrusions. Scale bar: 2μm.

(F) Quantification of MUC1 domains per AT2 cell in young adult mice (n = 3 mice). Data are presented as mean ±SEM. All MUC1 quantification was performed on 3D images.

(G and H) 3D rendering of immunostaining of AT2 (red), MUC1 (green), EZRIN (gray, G), and EPS-8 (gray, H). Scale bar: 2μm.

(I) Single stack and 3D rendering of AT2 (red), MUC1 (green), CDH1 (gray), and NKX2-1 (blue). 3D rendering is a representation of 24 z-slices. Dashed line indicates CDH1 domain. Scale bar, 3μm.

(J) Schematic representation of multi-alveolar enfacement of a single AT2 as well as alveoli with multiple AT2. Cell types as indicated. See also Figure S2 and Video S2.
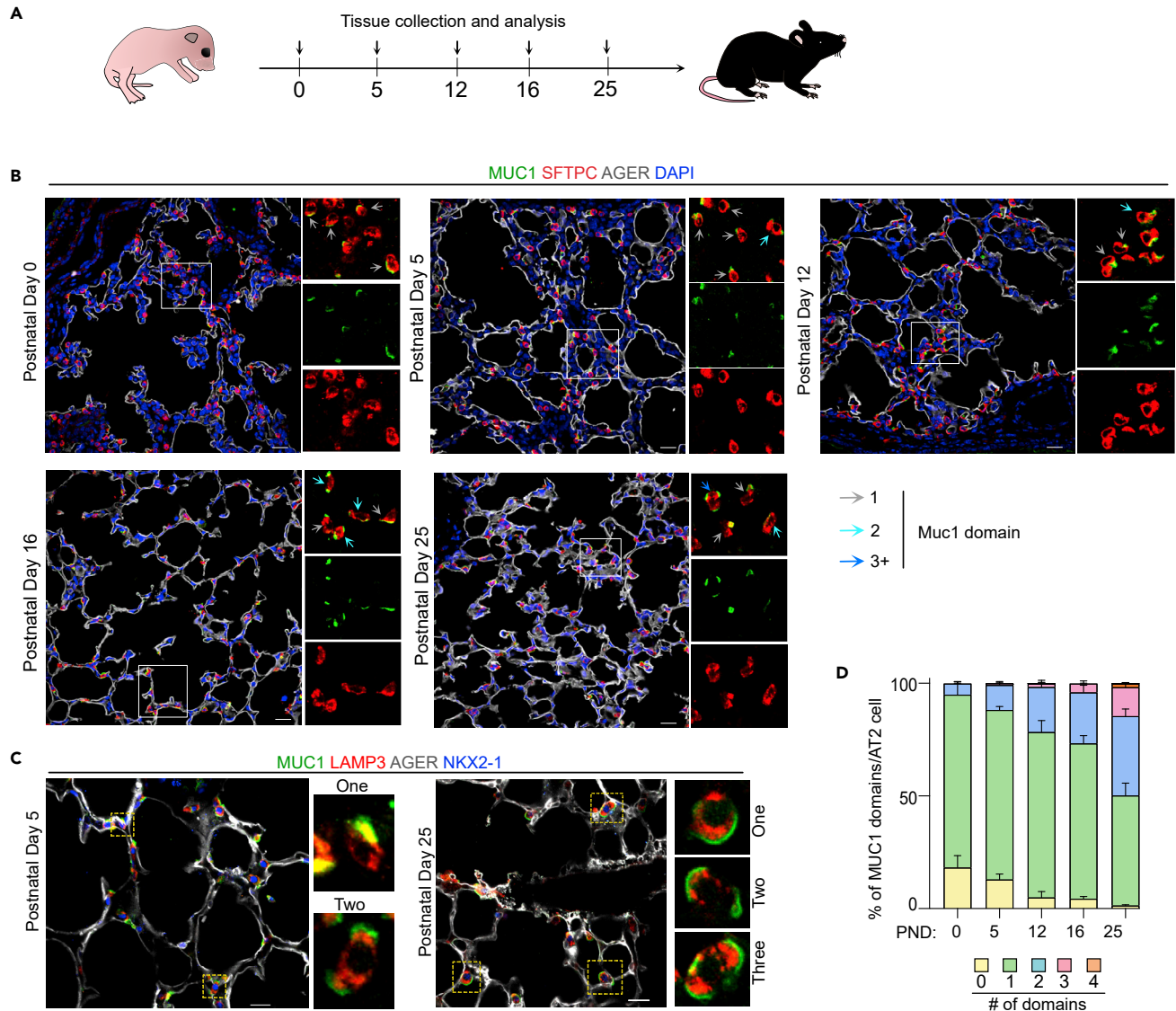
**Figure 3. AT2s gradually establish multiple apical domains during postnatal development**

(A) Experimental workflow for tissue collection of postnatal lungs.

(B) Immunostaining for MUC1 (green), SFTPC (red), and AGER (gray) in postnatal lungs. DAPI stains nuclei. Scale bar: 20μm. White boxed inset indicates enlarged single, or merge channels shown on right.

(C) Immunostaining for MUC1 (green), LAMP3 (red), AGER (gray) and NKX2-1 (blue) in postnatal day 5 and 25 lungs. DAPI stains nuclei. Scale bar: 20μm. White boxed inset indicates enlarged image with MUC1 and LAMP3 staining shown on right.

(D) Quantification of MUC1 domains/AT2 cell at indicated developmental stages (n = 3 mice/developmental time point). Data are presented as mean ±SEM. All MUC1 quantification was performed on 3D images.

3weeksat each round of ablation (Figures 4B and 4D). Of note, lineage tracing revealed that residual cells specifically contributed to AT2s but not AT1, suggesting that even after 3 rounds of ablation AT2s are able to sense the selective loss of specific cells and replenish neighboring alveoli by proliferation and migration.

We then tested whether AT2s can re-establish their localization pattern to enface multiple alveolar sacs following extensive proliferation and migration. To do so, we performed immunofluorescence on lungs collected 21 days after single, double, or triple ablation to visualize MUC1 domains. Our data from 3 rounds of AT2 ablated lungs revealed that AT2s that had proliferated (as visualized by based on BrdU incorporation) re-establish their localization to enface multiple alveolar sacs, a pattern similar to that of control lungs
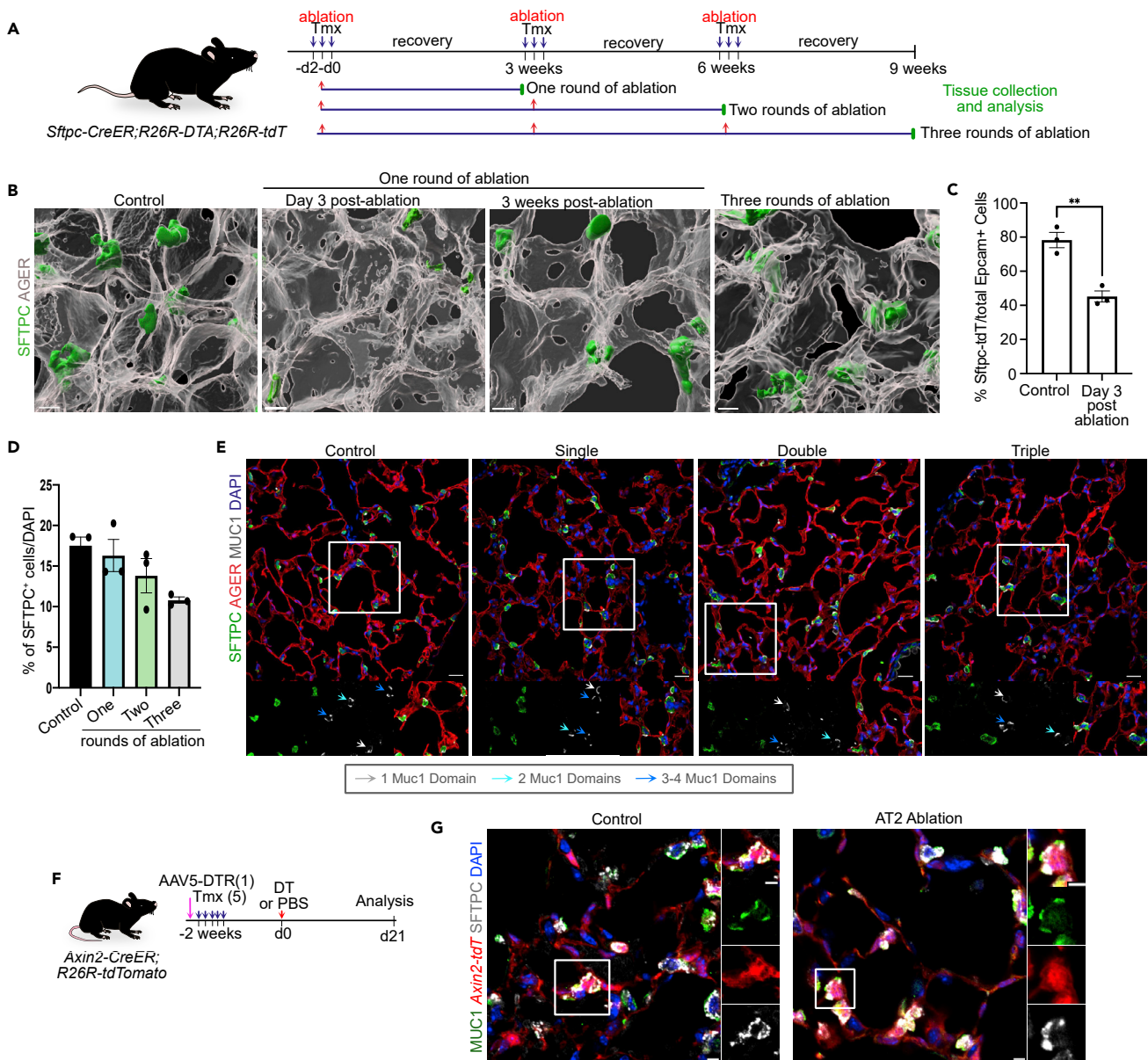
**Figure 4. Recovery and re-establishment of multipolar characteristics of AT2s after selective and repeated ablation**

(A) Schematic of experimental workflow of genetically induced single, double, and triple AT2 ablation in *Sftpc-CreER;R26R-DTA/R26R-tdT* mouse line.

(B) 3D rendered images of alveolar cups showing SFTPC (green) and AGER (gray) expressing cells in control, single ablation (day 3 and 3 weeks) and three rounds of AT2 ablated lungs. Scale bar: 10μm.

(C) Quantification of FACS-sorted AT2 numbers on day 3 post ablation, gated negatively for CD31/CD45 and normalized to total EPCAM+ cells. n = 3 mice/condition **p = 0.0039, two-tailed unpaired Student's *t* test, data are presented as mean ±SEM.

(D) Quantification of AT2 cell recovery three weeks post single, double, and three rounds of ablation, n = 3 mice/condition. One-way ANOVA, p = 0.0622. Data are presented as mean ±SEM.

(E) Immunostaining for MUC1 (gray), SFTPC (green), and AGER (red) on lung sections from control and 3 weeks post one , two, or three rounds of AT2 ablation. Insets: individual MUC1/SFTPC/AGER channels of regions indicated by white boxes. Gray arrows indicate single MUC1 domain, light blue 2+ MUC1 domains. DAPI stains nuclei. Scale bar: 20μm.

(F) Schematic of experimental workflow of tamoxifen induction and virus-mediated AT2 ablation in *Axin2-CreER;R26R-tdTomato* mice.

(G) Immunostaining for MUC1 (green), *Axin2-tdT* (red), and SFTPC (white) in control (left panel) and following AT2 ablation (right panel) in *Axin2-CreER;R26R-tdTomato* mice. Insets: individual and/or merged channels of regions indicated by boxes. DAPI stains nuclei. Scale bar: 20 μm. See also Figures S3 and S4.
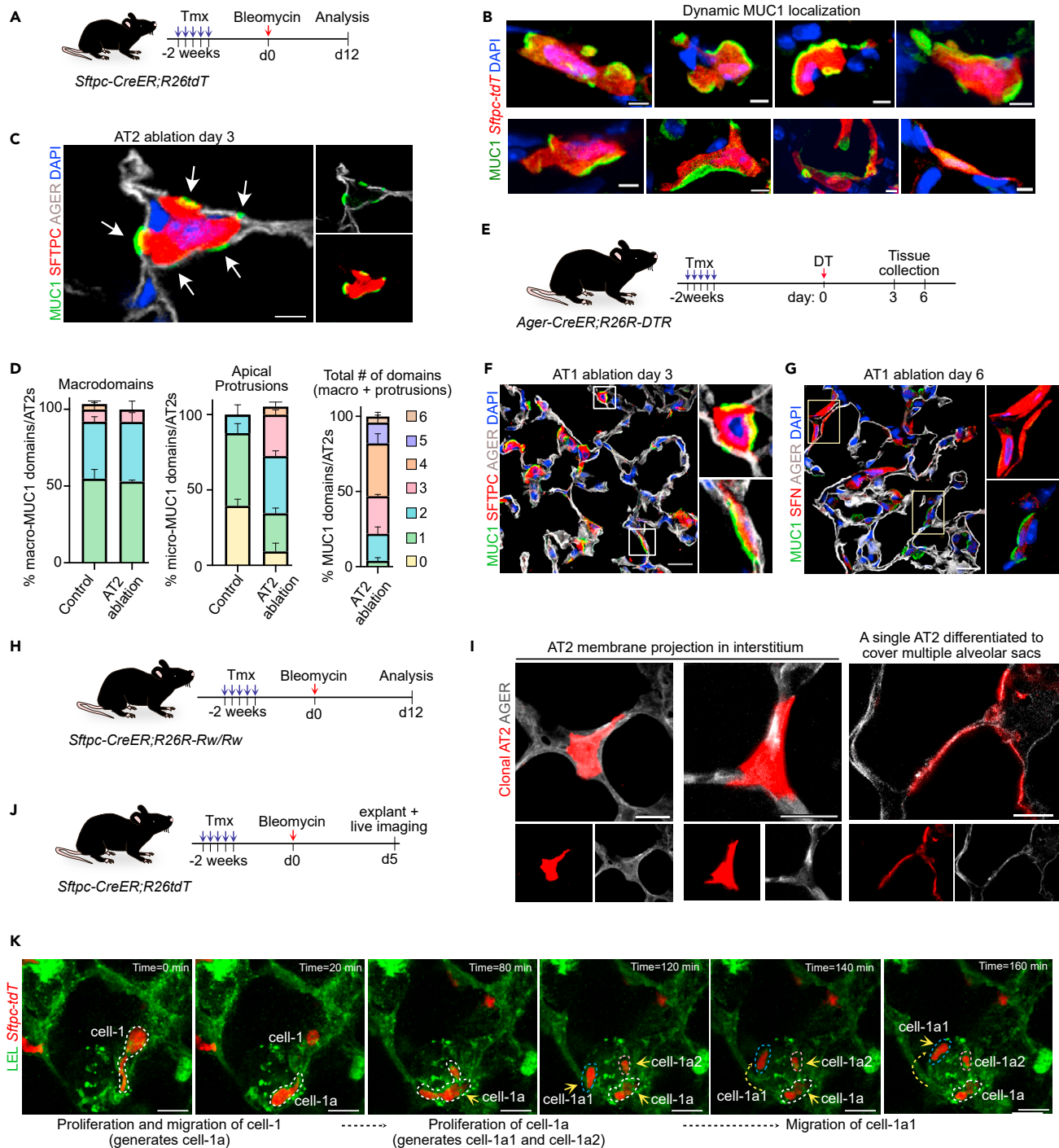
**Figure 5. Dynamics of AT2 apical domains during replication, migration, and differentiation**

(A) Experimental workflow for sequential administration of tamoxifen and bleomycin in *Sftpc-CreER;R26R-tdTomato* mice.

(B) Immunostaining of AT2s on bleomycin day 12, AT2 (red) and MUC1 (green). All scale bars: 20μm. DAPI stains nuclei.

(C) Immunostaining for MUC1 (green), SFTPC (red), and AGER (gray) at day 3 post AT2 ablation. Scale bar: 5μm.

(D) Quantification of total MUC1 domains (macro and micro) (left graph), macrodomains (middle graph), and apical protrusions (right graph) in control (n = 3 mice) and day 3 AT2-ablated lungs (n = 3 mice). All MUC1 quantification was performed on 3D images. For total MUC1 domains: two-way ANOVA (compared to controls shown in Figure 2F), ***p<0.0001. Sidak's multiple comparisons test as follows: 1 domain, p = 0.0811; 2 domains, **p = 0.0081; 3 domains, p = 0.9492; 4 domains, **p = 0.0028; 5 domains, p = 0.1360; 6 domains, p = 0.9303. For macrodomains: two-way ANOVA, p = 0.9242. For apical protrusions:

**Figure 5. Continued**

two-way ANOVA, ****p<0.0001. Sidak's multiple comparisons test as follows: 0 domains, ****p = 0.0002; 1 domain, **p = 0.0043; 2 domains, **p = 0.0014; 3 domains, ***p = 0.0007, 4 domains, p = 0.8962.

(E) Schematic depicting AT1 cell ablation using *Ager-CreER;R26R-DTR* mouse model. Sequential administration of tamoxifen (Tmx) and diphtheria toxin (DT) followed by tissue collection on day 3 and 6.

(F) Immunostaining for MUC1 (green), SFTPC (red), and AGER (gray) at day 3 post-AT1 ablation. Scale bar: 20μm.

(G) Co-staining for MUC1 (green), SFN (red), and AGER (gray) on day 6 following AT1 ablation. Scale bar: 20μm. Insets: individual and/or merged channels of regions indicated by boxes. DAPI stains nuclei.

(H) Experimental workflow for sequential administration of tamoxifen and bleomycin to *Sftpc-CreER;R26R-Rw/Rw* mice.

(I) Clonal AT2 (red) and AGER (gray) on day 12 following bleomycin. Images are 3D renderings or maximum intensity projections of 10–15 z-stacks. Scale bar: 20μm.

(J) Experimental workflow of live imaging following bleomycin injury.

(K) Snapshots from live imaging of lineage labeled AT2 cells (red) at indicated time points in bleomycin-injured lung. Alveoli outlined by LEL (green). Yellow arrow indicates membrane extension, proliferation and migration of lineage-labeled AT2 cell. Scale bar: 20μm. See also Figure S5, Videos S3 and S4.

(Figures 4E, S3C, and S3D). Importantly, we found cells containing all categories (i.e., single, double, and triple) of polar organization after multiple rounds of ablation (Figure 4E). We also observed a similar re-establishment of AT2 cell localization and MUC1 domains following AT2 ablation in 16-month-old mice (Figures S3E and S3F).

Previous studies have shown that a subset of AT2s is marked by Axin2 expression in adult lungs (Nabhan et al., 2018; Zacharias et al., 2018). We then tested whether there is any correlation between number of apical domains between Axin2-positive and negative AT2s. For this we used *Axin2-CreER;R26R-tdTomato* mice (in short, Axin2-tdT) to label Axin2-expressing cells and then examined their localization pattern and number of apical polar domains (Figure S4A). Co-immunostaining for MUC1, tdTomato, and SFTPC revealed that both Axin2-positive and negative AT2s show multi-lumen facing organization as well as multi-apical domains (Figures S4B and S4C). We then examined whether Axin2-expressing AT2s can reestablish multi-lumen enfacement and multi-apical polarity after injury. For this we utilized a recently developed adeno-associated viral (AAV) based approach, in which intranasal administration of AAV5-DTR virus selectively infects AT2s (A.K., Z.E., A.A., and P.R.T. manuscript in preparation) so that they can be ablated upon diphtheria toxin (DT) administration (Saito et al., 2001). We administered AAV5-DTR followed by DT to Axin2-tdT mice (Figure 4F). Analysis of lungs collected on day- 21 following DT administration revealed islands of Axin2-tdT lineage labeled cells, indicating that they had expanded to replenish lost cells (Figure S4E). Moreover, these Axin2$^+$ AT2s had re-established multi-apical polarity, just as Axin2$^-$ AT2s (Figure 4G). Together, these data reveal that AT2s can repopulate and re-establish multi-apical polarity to enface multiple alveolar sacs during injury repair.

## AT2s dynamically reorganize multi-apical domains during injury repair

To understand apical membrane dynamics following alveolar injury, we labeled AT2s with tdTomato using Sftpc-tdT mice followed by administration of bleomycin to cause lung damage (Figure 5A). Immunostaining for MUC1 and tdTomato on day-12 post bleomycin revealed cells with distinct apical domain patterns suggesting their reorganization after injury (Figures 5B and 5C). Broadly, we identified two major MUC1 localization patterns: AT2s with numerous MUC1 enriched small protrusions, as well as stretched cells with elongated MUC1 domains along the luminal surface (Figure 5B). Notably, fully stretched AT2s lost MUC1 expression (Figure 5B, bottom right panel). To determine whether these patterns are correlated with AT2 renewal/migration or with differentiation in AT1s, we performed selective ablation of AT2s and AT1s. First, after selectively ablating AT2s we assessed whether the surviving (residual) AT2s, that proliferate and migrate, change the numbers and localization of their apical domains. For this, we performed immunostaining for MUC1 on day 3 after AT2 ablation, at which time a significant number of residual AT2s are undergoing replication (Figures S3A and S3B). Interestingly, we observed dramatic changes in MUC1 localization pattern. Specifically, the majority of residual AT2s increased the number of their multi-apical domains, ranging from 1 to 6 as opposed to 1–4 in controls (Figures 5C and S5A). Moreover, the number of apical protrusions was significantly increased compared to controls, whereas the number of macrodomains remain unchanged (Figure 5D).

Second, we assessed the MUC1 localization pattern in AT2s during their differentiation into AT1s. For this, we used an *Ager-CreER;R26R-LSL-DTR* (in short, Ager-DTR) mouse model, in which administration of tamoxifen followed by DT leads to selective ablation of AT1s (Figure 5E). In this model, AT2s rapidly
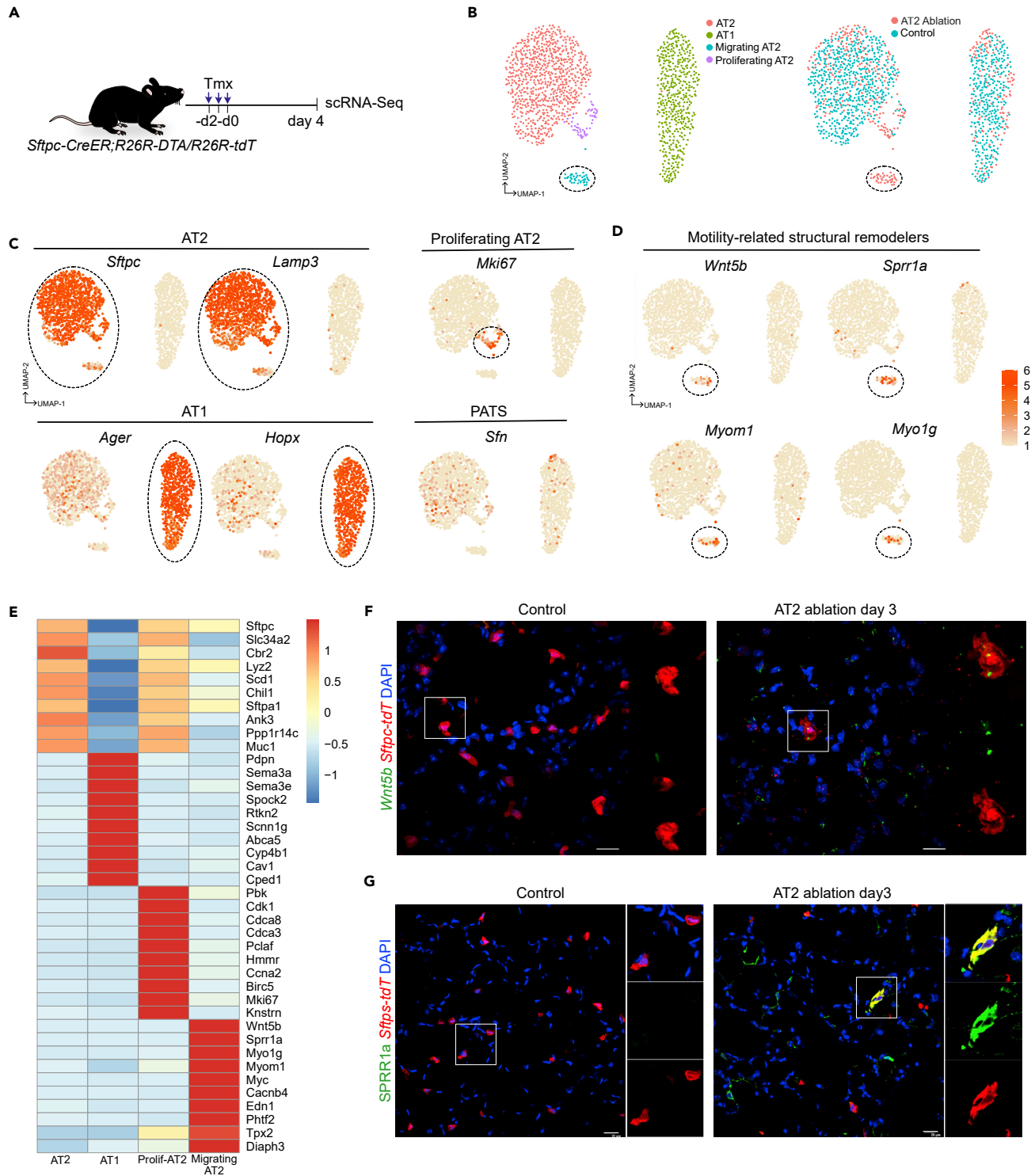
**Figure 6. Distinct and unique gene expression profiles define an injury-specific, migrating AT2 population**

(A) Experimental workflow to ablate AT2 cells in *Sftpc-CreER;R26R-DTA/R26-tdT* mice, followed by cell capture and single cell transcriptome sequencing.

(B) UMAPs show alveolar epithelial cell populations in control and day 4 after AT2 ablation.

(C) UMAPs show expression of indicated genes in AT2, proliferating AT2, AT1 and PATS. Dotted line circles indicate enrichment of indicated genes in UMAPs.

**Figure 6. *Continued***
(D) UMAPs show expression of indicated genes in migrating AT2s (dashed circle).
(E) Heatmap shows relative expression of indicated genes in alveolar epithelial cell populations.
(F) PLISH for *Wnt5b* (green) and *Sftpc-tdT* (red) in control and day 3 after AT2 ablation.
(G) Immunostaining for SPRR1A (green) and *Sftpc-tdT* in control and day 3 following AT2 ablation. DAPI stains nuclei. Scale bar: 20μm. Enlarged image from inset is shown on the right. See also Figure S6, Tables S1, S2, and S3.

differentiate into AT1 via a recently described transitional state (Choi et al., 2020; Kobayashi et al., 2020; Strunz et al., 2020). Co-immunostaining for MUC1, SFTPC, and AGER on lung sections collected on day-3 post AT1 ablation revealed that the MUC1 localization pattern changed from localized discs/small patches to a much more extensive sheets covering the luminal surface of the stretched AT2s (Figure 5F). To test whether this MUC1 localization pattern is also present in the transitional state, we performed immunostaining for MUC1 and the cytoplasmic protein, stratifin (SFN), a marker for transitional states, on lung tissues collected 6 days after AT1 ablation. We observed no co-expression of MUC1 and SFN in alveolar epithelial cells (Figure 5G). These data suggest that AT2s dynamically reorganize MUC1 localization and eventually downregulate its expression as they acquire a transitional state *en route* to differentiation.

To determine morphological changes associated with individual AT2s during their migration and differentiation, we clonally labeled AT2s using *Sftpc-CreER;R26R-Raimbow* mice (in short, *Sftpc-CreER;R26R-Rw*) followed by administration of bleomycin to cause lung injury (Figure 5H). Visualization of clonally labeled AT2s revealed different morphological changes associated with cell migration and differentiation. We found elongated AT2s with distinct membrane protrusions, which likely represent migrating cells (Figure 5I, left and middle panel). Additionally, consistent with previous studies (Desai et al., 2014), we observed a single clonally labeled AT2 differentiated into AT1 cell that covered multiple neighboring alveolar sacs (Figure 5I, right panel and Figures S5B and S5C).

To further visualize AT2 migration, we used the *Sftpc-creER;R26R-tdT* mouse model and administered bleomycin followed by live-imaging of agarose-inflated, explanted, lung lobes. We observed proliferation of residual cells and migration of daughter AT2s as visualized by tdTomato lineage label (Figures 5J, 5K, and S5E, Videos S3 and S4). Notably, we found that AT2s are highly dynamic and migrate following injury. Taken together, these data reveal that a single AT2 cell can replicate and migrate to repopulate AT2s in neighboring alveolar sacs.

## scRNA-seq reveals enhanced cytoskeletal and cell signaling dynamics in migrating AT2s

To investigate the mechanisms contributing to the proliferation and recovery of surviving AT2s, after their bulk ablation, we performed single cell transcriptome analysis. For this, we isolated and enriched epithelial and mesenchymal cells from control and day 4 after AT2 ablated lungs and performed droplet based single cell capture and RNA library preparation (Figure 6A). Integration of control and ablated lungs followed by uniform manifold approximation and projection (UMAP) of the alveolar epithelium identified known cell types, including AT2s (*Sftpc* and *Lamp3*), AT1s (*Ager* and *Hopx*), and proliferating AT2s (*Ki67* and *Top2a*) (Figures 6B and 6C). Significantly, we observed a cell cluster that originated solely from AT2-ablated lungs but not from control lungs (Figure 6B). Of note, we did not find pre-AT1 transitional states (PATS) as evidenced by the lack of expression of *Sfn*, *Fn1*, *Cldn4*, and *Ctgf* (Figures 6C and Table S1). The cell cluster unique to ablated lungs was enriched for *Wnt5b*, *Sprr1a*, *Myo1g*, *Myom1*, *Myc*, *Cacnb4*, *Edn1*, *Phtf2*, *Tpx2*, *and Diaph3,* all of which are known regulators of cell migration (Aragona et al., 2020; Cruz-Zárate et al., 2021; Dekoninck and Blanpain, 2019; Harada et al., 2017; Strunz et al., 2020) (Figures 6B–6E and S6A–S6D, Tables S2 and S3). Therefore, we termed this cluster "migratory AT2s" (Figures 6B–6F). We also observed significant downregulation of *Sftpc* transcripts in migratory AT2s compared to other AT2s and proliferating AT2s (Figure S6E) and validated this observation by immunostaining for SFTPC following AT2 ablation (Figure S6F). Proximity ligation *in situ* hybridization or immunostaining analysis in conjunction with the AT2-lineage tracing reporter tdTomato on day-3 post ablation revealed expression of *Wnt5b* transcripts and SPRR1A protein (a small proline-rich protein, expressed in differentiating keratinocytes), respectively, only in residual AT2s from ablated lungs but not in controls (Figures 6F and 6G). Of note, we also observed significant enrichment of *Wnt5b* transcripts in other cell types in the alveoli of ablated lungs but not in controls, suggesting that other cell populations are involved in the recovery of alveolar architecture after loss of AT2s, presumably through promoting the replication and migration of residual AT2s. (Figure 6F). To determine whether migrating cells had unique membrane dynamics, we also analyzed
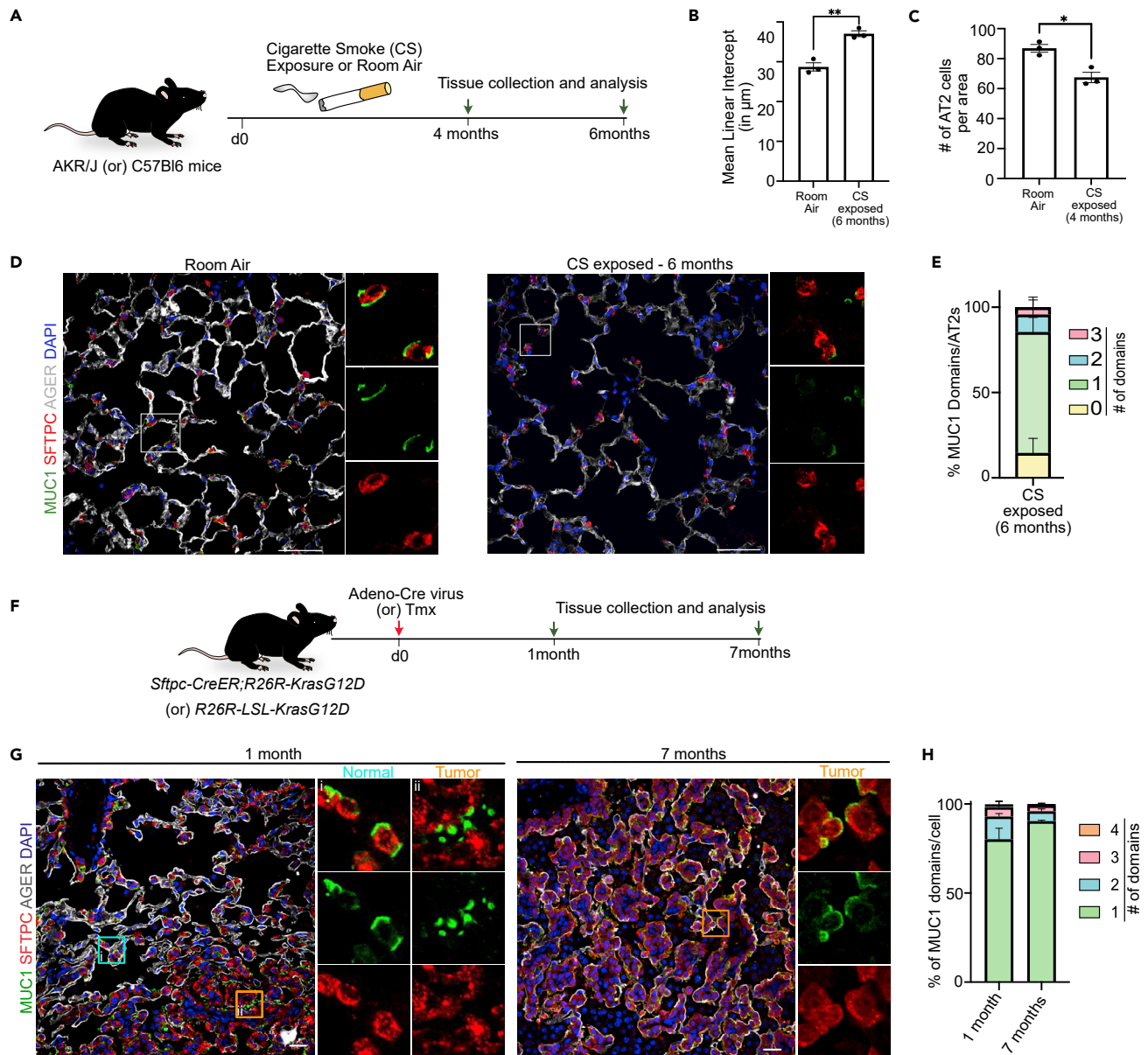
**Figure 7. Smoking and oncogenic events disrupt multi-apical domain organization in AT2s**

(A) Schematic depicting cigarette smoke (CS) exposure and tissue collection.

(B) Mean linear intercept of room air exposed or 6-month CS exposed mice. n = 3 mice/condition, **p = 0.0027, two-tailed unpaired Student's *t* test, data are presented as mean ± SEM.

(C) Quantification of AT2 cell numbers per area in room-air or CS-exposed mice. n = 3 mice, *p = 0.041, two-tailed unpaired Student's *t* test. Data are presented as mean ± SEM.

(D) Immunostaining for MUC1 (green), SFTPC (red), and AGER (gray) on room-air (control), CS-exposed (6-month) mouse lungs. Scale bar: 20μm.

(E) Quantification of MUC1 domains in 6-month CS-exposed mice. n = 3 mice. All MUC1 quantification was performed on 3D sections. Data are presented as mean ± SEMSEM. Two-way ANOVA (compared to control data from Figure 2F), **p = 0.0035. Sidak's multiple comparisons test: as follows: 0 domains, p = 0.3817; 1 domain, ****p<0.0001; 2 domains, **p = 0.0079; 3 domains, *p = 0.0195; 4 domains, p = 0.6180.

(F) Schematic depicting oncogene activation either by tamoxifen injection (*Sftpc-CreER; R26R-LSL-Kras*[G12D]) or cre transduction using adenovirus (*R26R-LSL-Kras*[G12D]) followed by tissue collection and analysis.

(G) Immunostaining for MUC1 (green), SFTPC (red), and AGER (gray) on lungs from 1- and 7-month following oncogene activation. Insets: individual MUC1/SFTPC and merged channels of regions indicated by boxes. (1) normal lung (light blue box) (2) tumor (orange box). DAPI stains nuclei. Scale bar: 20μm.

**Figure 7. Continued**

(H) Quantification of MUC1 domains in early and late-stage tumor mice. n = 3 mice/condition. All MUC1 quantification was performed on 3D sections. Data are presented as mean ±SEM. Two-way ANOVA (compared with homeostatic mice, Figure 1F), ****p<0.0001. Sidak's multiple comparisons test as follows: 1 domain, Homeostasis versus Early tumor, ****p<0.0001. Homeostasis versus Late tumors, ****p<0.0001. Early tumor versus Late tumors, p = 0.0871; 2 domains, Homeostasis versus Early tumor, ****p<0.0001. Homeostasis versus Late tumors, ****p<0.0001. Early tumor versus Late tumors, p = 0.2779; 3 domains, Homeostasis versus Early tumor, ****p<0.0001. Homeostasis versus Late tumors, ****p<0.0001. Early tumor versus Late tumors, p = 0.9129. Homeostasis versus Early tumor, p = 0.0906. Homeostasis versus Late tumors, p = 0.0555. Early tumor versus Late tumors, p = 0.9702. See also Figure S7.

the MUC1 domains of SPRR1A^{+} cells 3 days after AT2 ablation (Figures S6G and S6H). Of interest, SPRR1A^{+} AT2s contained more MUC1 domains (both macro and apical protrusions) as compared to AT2s from homeostatic lungs, but there was no significant difference between SPRR1A +ve and-ve cells. Gene expression signatures further revealed enrichment of autophagy, mitophagy, cytoskeletal regulation, TNF signaling, tight junction remodeling, MAPK signaling, and spliceosome pathways specifically in migratory AT2s but not in other AT2s from ablated lungs as well as control lungs (Figures 6B and S6A, Tables S2 and S3). These data suggest that residual AT2s activate a migratory program to promote recovery of lost cells in AT2 ablated lungs.

### Smoking and oncogenic events disrupt multi-apical domain organization in AT2s

Various environmental and genetic factors are known to alter the self-renewal and differentiation potential of AT2s during homeostasis and repair after injury (Baumgartner et al., 1997; Rock et al., 2010; Rock and Hogan, 2011; Wilson et al., 1960). To test whether such genetic and environmental factors influence the multipolarity of AT2s, we either exposed mice to cigarette smoke (CS) to induce alveolar damage or activated an oncogene specifically in AT2s. Mice were exposed to CS for 4 or 6 months (see STAR methods for details) followed by tissue collection and analysis. Room air exposed mice were used as controls (Figure 7A). As expected, lungs begin to show enlarged air spaces, a characteristic feature of emphysema, by 4 months after CS exposure as revealed by hematoxylin and eosin staining (Figures 7B and S7A). These structural alterations were more apparent by 6 months after CS exposure. Co-immunostaining for SFTPC, AGER, and MUC1 revealed the presence of both AT2 and AT1 cells. However, we observed a significant (32%) decrease in the number of AT2s in CS exposed lungs compared to controls (Figures 7C, 7D, and S7B). In addition, we observed a diffuse pattern of MUC1 localization in the damaged regions of CS exposed lungs as opposed to multi-apical localization in control lungs and undamaged regions of CS exposed lungs. These data suggest that smoke exposure disrupts multi-apical characteristics of residual AT2s (Figures 7A–7E, S7A, and S7B).

Next, we tested whether the multi-apical domain organization of AT2s is disrupted following activation of an oncogene. As shown in Figure 7F, we constitutively expressed *Kras* (G12D), a mutant form of Ras GTPase that is known to induce hyper replication in AT2s and block their ability to differentiate into AT1s(Jackson et al., 2001; Tuveson et al., 2004), and collected lungs at 1 month and 7 months after activation. Of note, these times correlate with adenoma and adenocarcinoma stages of lung tumorigenesis, respectively. As expected, co-immunostaining for SFTPC, AGER, and MUC1 revealed densely packed SFTPC-expressing, oncogene-activated AT2-like cells in both adenomas and adenocarcinomas (Figure 7G). Of interest, we found altered patterns of MUC1 localization in both locations, whereas the AT2s in adjacent regions showed normal multi-apical polarity. In both adenomas and adenocarcinomas, we observed a decrease in overall MUC1 domains, in which the majority of oncogene-activated AT2-like cells were uni-polar (Figure 7H). Taken together, these findings suggest that both cigarette smoking and oncogene activation leads to disruption of the multi-apical polarity characteristic of normal.

## DISCUSSION

Respiratory organs in vertebrates have evolved a highly compartmentalized tissue organization to facilitate increased surface area and efficient gas exchange to satisfy oxygen demands. Here we describe a unique cellular organization of the AT2 cells of the lung alveolus. Our high-resolution light and electron microscopy imaging and developmental studies have revealed that AT2s develop a unique, multi-apical domain architecture. Our study not only re-evaluates previous observations from the 1970's that a single AT2 project into multiple alveoli, but also provides insights into the multi-apical polarity organization of these cells (Cordingley, 1972; Weibel, 1971). Of significance, these apical domains can face up to 4 different alveolar sacs in cells located at the intersection of multiple alveoli. We propose that this architecture enables individual AT2s to monitor the integrity of multiple alveolar sacs and to be poised to respond as necessary to the loss of either

AT2 or AT1 cell. Furthermore, we also speculate that such multi-apical polarity may facilitate the secretion of surfactants by a single AT2 into multiple alveolar sacs. This model of AT2 organization revises prevailing depictions in the current literature in which AT2s are attached to the alveolar basement membrane with their cell bodies protruding into the lumen of a single alveolus. This model provides a framework for explaining how a single AT2-derived AT1 can contribute to covering multiple alveolar sacs during differentiation.

Following alveolar injury, AT2s demonstrate the ability to reorganize their apical domains during replication, migration, and differentiation-associated cell stretching. Remarkably, AT2s appear to acquire more apical protrusions during replication and migration. This suggests that AT2s reorganize their cell membranes during replication and "prime" themselves to reestablish macrodomains at any region of the membrane. Together, these unique characteristics of AT2s defy the classical definition of an epithelial cell with a defined shape and with static apical and basolateral domains.

Our data also demonstrate that AT2s have the tremendous regenerative capacity even after extensive damage. Indeed, we show that AT2s can replicate and migrate to replenish lost cells in multiple neighboring alveoli even after three rounds of cell ablation. Moreover, AT2s are able to re-establish their multi-apical polarity during regeneration. Our study thus provides direct evidence for the self-organizing property of AT2s and, therefore, has significant implications for translational applications in pulmonary medicine, such as cell engraftment and lung tissue engineering.

Molecularly, our single-cell transcriptome analysis has revealed significant enrichment of transcripts associated with cell migration and actin cytoskeletal dynamics. Nevertheless, it remains unknown whether AT2s use specialized protein complexes and membrane sorting mechanisms for establishing their multi-apical domains. This will be a topic of interest for future studies. Finally, our study also implies that dysregulation of multi-apical polarity characteristics of alveolar stem cells may underlie clinically relevant diseases. For example, AT2s either completely lose or disorganize their multi-apical domains after cigarette smoke exposure, a hazard that leads to emphysema. Similarly, oncogene activated AT2s show disorganized apical domains, increasingly becoming unipolar at later stages, suggesting that the multi-apical polarity of AT2s is dynamically regulated in normal as well as disease states. Indeed, genetic mutations or altered expression of MUC1 has been implicated in lung cancer growth, metastasis, and chemotherapy resistance (Bouillez et al., 2016; Ham et al., 2016; Horimasu et al., 2017; Raina et al., 2011; Saltos et al., 2018). In sum, our study has uncovered a unique multi-apical polarity of an epithelial cell type and its dynamics during development, injury repair, and tumorigenesis.

## Limitations of this study

This study revealed a unique multi-apical polarity and multi-lumen enfacement organization of alveolar stem cells. Our data from clonal lineage tracing following injury suggests that such organization allows AT2s to differentiate into AT1s that can spread and cover multiple adjacent alveolar sacs. However, these data require further analysis such as live imaging to visualize spreading of a single AT2 cell into multiple alveolar sacs. Current microscopy methods for visualizing alveolar regeneration are not suitable for such long-term imaging. In addition, differentiating AT2s have extremely thin cell bodies and cell membrane and therefore visualization of spreading cells is difficult over time due to photobleaching. Our data also suggest that multi-apical domains of AT2s dynamically reorganize during injury repair. However, one limitation is that these conclusions are based on data from static images collected at different times and tissue regions. Further work needs to focus on developing stable fluorescence probes and new imaging modalities to visualize alveolar regeneration over multiple days.

To our knowledge, this study reports the first description of multi-apical polar organization in any epithelial tissue but currently we do not know the specific regulators of such unique polarity organization. Identification and perturbation of such regulators will enable disruption of multi-apical polarity (but not uni-polarity) of AT2s so that the consequences with respect to their regenerative potential can be followed. Lastly, although we found oncogenic mechanisms disrupt multi-apical polarity of AT2s, whether such dysregulation is specific to multi-apical polarity or also includes general uni-polarity remains unknown. As alluded to above, identification of specific regulators of multi-apical polarity is needed to address these questions. Furthermore, uncovering such mechanisms will enhance our understanding of how cell polarity in general contributes to tissue organization and regeneration, and the significance of its disruption in disease.

## STAR★METHODS

Detailed methods are provided in the online version of this paper and include the following:

- KEY RESOURCES TABLE
- RESOURCE AVAILABILITY
  - Lead contact
  - Materials availability
  - Data and code availability
- EXPERIMENTAL MODEL AND SUBJECT DETAILS
  - Animals
  - Human lung tissue
- METHOD DETAILS
  - Tissue preparation and sectioning
  - Immunofluorescence staining
  - Plasmid construction, AAV production
  - Live imaging of explanted lungs
  - Electron microscopy of lung tissue
  - Mouse lung tissue dissociation and cell isolation
  - Single-cell sequencing via 10Xgenomics
  - Proximity ligation *in situ* hybridization (PLISH)
  - *In vivo* cigarette smoke (CS) exposure
  - Statistical analysis
  - Image acquisition and processing

## SUPPLEMENTAL INFORMATION

Supplemental information can be found online at https://doi.org/10.1016/j.isci.2022.105114.

## AUTHOR CONTRIBUTIONS

A.K. co-designed, conceived, and performed the experiments, analyzed data and co-wrote the manuscript; S.K. designed and performed experiments and assisted with imaging. P.K.L.M and Y.K. performed single-cell RNA-sequencing and assisted in computational analysis. Z.C.E., A.A., and A.M.P. provided reagents. S.K. and P.J.L. performed smoking exposures. A.M. and J.J.B-C performed live imaging. L.K. performed transmission electron microscopy. A.T. and P.R.T. co-designed, conceived and supervised the work and co-wrote the manuscript. All authors reviewed and edited the manuscript.

## DECLARATION OF INTERESTS

P.R.T. serves as acting CEO of Iolux Inc. P.R.T. serves as a consultant for Surrozen Inc., Cellarity Inc., and Celldom Inc., on work unrelated to the contents of this manuscript. A.A. is a founder and board director at StrideBio Inc. and Torque Bio Inc. as well as serves as a scientific advisor to Kriya Therapeutics, Atsena

## REFERENCES

Aragona, M., Sifrim, A., Malfait, M., Song, Y., Van Herck, J., Dekoninck, S., Gargouri, S., Lapouge, G., Swedlund, B., Dubois, C., et al. (2020). Mechanisms of stretch-mediated skin expansion at single-cell resolution. Nature 584, 268–273. https://doi.org/10.1038/s41586-020-2555-7.

Barkauskas, C.E., Cronce, M.J., Rackley, C.R., Bowie, E.J., Keene, D.R., Stripp, B.R., Randell, S.H., Noble, P.W., and Hogan, B.L.M. (2013). Type 2 alveolar cells are stem cells in adult lung. J. Clin. Invest. 123, 3025–3036. https://doi.org/10.1172/JCI68782.

Basil, M.C., Katzen, J., Engler, A.E., Guo, M., Herriges, M.J., Kathiriya, J.J., Windmueller, R., Ysasi, A.B., Zacharias, W.J., Chapman, H.A., et al. (2020). The cellular and physiological basis for lung repair and regeneration: past, present, and future. Cell Stem Cell 26, 482–502. https://doi.org/10.1016/j.stem.2020.03.009.

Baumgartner, K.B., Samet, J.M., Stidley, C.A., Colby, T.V., and Waldron, J.A. (1997). Cigarette smoking: a risk factor for idiopathic pulmonary fibrosis. Am. J. Respir. Crit. Care Med. 155, 242–248. https://doi.org/10.1164/ajrccm.155.1.9001319.

Beike, L., Wrede, C., Hegermann, J., Lopez-Rodriguez, E., Kloth, C., Gauldie, J., Kolb, M., Maus, U.A., Ochs, M., and Knudsen, L. (2019). Surfactant dysfunction and alveolar collapse are linked with fibrotic septal wall remodeling in the TGF-β1-induced mouse model of pulmonary fibrosis. Lab. Invest. 99, 830–852. https://doi.org/10.1038/s41374-019-0189-x.

Blanpain, C., and Fuchs, E. (2014). Stem cell plasticity. Plasticity of epithelial stem cells in tissue regeneration. Science 344, 1242281. https://doi.org/10.1126/science.1242281.

Bouillez, A., Rajabi, H., Pitroda, S., Jin, C., Alam, M., Kharbanda, A., Tagde, A., Wong, K.-K., and Kufe, D. (2016). Inhibition of MUC1-C suppresses MYC expression and attenuates malignant growth in KRAS mutant lung adenocarcinomas. Cancer Res. 76, 1538–1548. https://doi.org/10.1158/0008-5472.CAN-15-1804.

Branchfield, K., Li, R., Lungova, V., Verheyden, J.M., McCulley, D., and Sun, X. (2016). A three-dimensional study of alveologenesis in mouse lung. Dev. Biol. 409, 429–441. https://doi.org/10.1016/j.ydbio.2015.11.017.

Buch, T., Heppner, F.L., Tertilt, C., Heinen, T.J.A.J., Kremer, M., Wunderlich, F.T., Jung, S., and Waisman, A. (2005). A Cre-inducible diphtheria toxin receptor mediates cell lineage ablation after toxin administration. Nat. Methods 2, 419–426. https://doi.org/10.1038/nmeth762.

Cardoso, W.V., and Lü, J. (2006). Regulation of early lung morphogenesis: questions, facts and controversies. Development 133, 1611–1624. https://doi.org/10.1242/dev.02310.

Cardoso, W.V., and Whitsett, J.A. (2008). Resident cellular components of the lung: developmental aspects. Proc. Am. Thorac. Soc. 5, 767–771. https://doi.org/10.1513/pats.200803-026HR.

Choi, J., Park, J.-E., Tsagkogeorga, G., Yanagita, M., Koo, B.-K., Han, N., and Lee, J.-H. (2020). Inflammatory signals induce AT2 cell-derived damage-associated transient progenitors that mediate alveolar regeneration. Cell Stem Cell 27, 366–382.e7. https://doi.org/10.1016/j.stem.2020.06.020.

Chung, M.-I., Bujnis, M., Barkauskas, C.E., Kobayashi, Y., and Hogan, B.L.M. (2018). Niche-mediated BMP/SMAD signaling regulates lung alveolar stem cell proliferation and differentiation. Development 145, dev163014. https://doi.org/10.1242/dev.163014.

Clevers, H., Loh, K.M., and Nusse, R. (2014). Stem cell signaling. An integral program for tissue renewal and regeneration: Wnt signaling and stem cell control. Science 346, 1248012. https://doi.org/10.1126/science.1248012.

Clevers, H., and Watt, F.M. (2018). Defining adult stem cells by function, not by phenotype. Annu. Rev. Biochem. 87, 1015–1027. https://doi.org/10.1146/annurev-biochem-062917-012341.

Cordingley, J.L. (1972). Pores of Kohn. Thorax 27, 433–441. https://doi.org/10.1136/thx.27.4.433.

Cruz-Zárate, D., López-Ortega, O., Girón-Pérez, D.A., Gonzalez-Suarez, A.M., García-Cordero, J.L., Schnoor, M., and Santos-Argumedo, L. (2021). Myo1g is required for efficient adhesion and migration of activated B lymphocytes to inguinal lymph nodes. Sci. Rep. 11, 7197. https://doi.org/10.1038/s41598-021-85477-y.

Dekoninck, S., and Blanpain, C. (2019). Stem cell dynamics, migration and plasticity during wound healing. Nat. Cell Biol. 21, 18–24. https://doi.org/10.1038/s41556-018-0237-6.

Desai, T.J., Brownfield, D.G., and Krasnow, M.A. (2014). Alveolar progenitor and stem cells in lung development, renewal and cancer. Nature 507, 190–194. https://doi.org/10.1038/nature12930.

DuPage, M., Dooley, A.L., and Jacks, T. (2009). Conditional mouse lung cancer models using adenoviral or lentiviral delivery of Cre recombinase. Nat. Protoc. 4, 1064–1072. https://doi.org/10.1038/nprot.2009.95.

Fuchs, E., and Blau, H.M. (2020). Tissue stem cells: architects of their niches. Cell Stem Cell 27, 532–556. https://doi.org/10.1016/j.stem.2020.09.011.

Fuchs, Y., and Steller, H. (2015). Live to die another way: modes of programmed cell death and the signals emanating from dying cells. Nat. Rev. Mol. Cell Biol. 16, 329–344. https://doi.org/10.1038/nrm3999.

Ham, S.Y., Kwon, T., Bak, Y., Yu, J.-H., Hong, J., Lee, S.K., Yu, D.-Y., and Yoon, D.-Y. (2016). Mucin 1-mediated chemo-resistance in lung cancer cells. Oncogenesis 5, e185. https://doi.org/10.1038/oncsis.2015.47.

Harada, T., Yamamoto, H., Kishida, S., Kishida, M., Awada, C., Takao, T., and Kikuchi, A. (2017). Wnt5b-associated exosomes promote cancer cell migration and proliferation. Cancer Sci. 108, 42–52. https://doi.org/10.1111/cas.13109.

Herriges, M., and Morrisey, E.E. (2014). Lung development: orchestrating the generation and regeneration of a complex organ. Development 141, 502–513. https://doi.org/10.1242/dev.098186.

Hogan, B.L.M., Barkauskas, C.E., Chapman, H.A., Epstein, J.A., Jain, R., Hsia, C.C.W., Niklason, L., Calle, E., Le, A., Randell, S.H., et al. (2014). Repair and regeneration of the respiratory system: complexity, plasticity, and mechanisms of lung stem cell function. Cell Stem Cell 15, 123–138. https://doi.org/10.1016/j.stem.2014.07.012.

Horimasu, Y., Ishikawa, N., Tanaka, S., Hirano, C., Iwamoto, H., Ohshimo, S., Fujitaka, K., Hamada, H., Hattori, N., and Kohno, N. (2017). MUC1 in lung adenocarcinoma: cross-sectional genetic and serological study. BMC Cancer 17, 263. https://doi.org/10.1186/s12885-017-3272-y.

Hsu, Y.-C., Pasolli, H.A., and Fuchs, E. (2011). Dynamics between stem cells, niche, and progeny in the hair follicle. Cell 144, 92–105. https://doi.org/10.1016/j.cell.2010.11.049.

Huang, T., You, Y., Spoor, M.S., Richer, E.J., Kudva, V.V., Paige, R.C., Seiler, M.P., Liebler, J.M., Zabner, J., Plopper, C.G., and Brody, S.L. (2003). Foxj1 is required for apical localization of ezrin in

airway epithelial cells. J. Cell Sci. *116*, 4935–4945. https://doi.org/10.1242/jcs.00830.

Ivanova, A., Signore, M., Caro, N., Greene, N.D.E., Copp, A.J., and Martinez-Barbera, J.P. (2005). In vivo genetic ablation by Cre-mediated expression of diphtheria toxin fragment A. Genesis *43*, 129–135. https://doi.org/10.1002/gene.20162.

Jackson, E.L., Willis, N., Mercer, K., Bronson, R.T., Crowley, D., Montoya, R., Jacks, T., and Tuveson, D.A. (2001). Analysis of lung tumor initiation and progression using conditional expression of oncogenic K-ras. Genes Dev. *15*, 3243–3248. https://doi.org/10.1101/gad.943001.

Katsura, H., Sontake, V., Tata, A., Kobayashi, Y., Edwards, C.E., Heaton, B.E., Konkimalla, A., Asakura, T., Mikami, Y., Fritch, E.J., et al. (2020). Human lung stem cell-based alveolospheres provide insights into SARS-CoV-2 mediated interferon responses and pneumocyte dysfunction. Cell Stem Cell *27*, 890–904.e8. https://doi.org/10.1016/j.stem.2020.10.005.

Knust, J., Ochs, M., Gundersen, H.J.G., and Nyengaard, J.R. (2009). Stereological estimates of alveolar number and size and capillary length and surface area in mice lungs. Anat. Rec. *292*, 113–122. https://doi.org/10.1002/ar.20747.

Kobayashi, Y., Tata, A., Konkimalla, A., Katsura, H., Lee, R.F., Ou, J., Banovich, N.E., Kropski, J.A., and Tata, P.R. (2020). Persistence of a regeneration-associated, transitional alveolar epithelial cell state in pulmonary fibrosis. Nat. Cell Biol. *22*, 934–946. https://doi.org/10.1038/s41556-020-0542-8.

Konishi, S., Tata, A., and Tata, P.R. (2022). Defined conditions for long-term expansion of murine and human alveolar epithelial stem cells in three-dimensional cultures. STAR Protoc. *3*, 101447. https://doi.org/10.1016/j.xpro.2022.101447.

Kuleshov, M.V., Jones, M.R., Rouillard, A.D., Fernandez, N.F., Duan, Q., Wang, Z., Koplev, S., Jenkins, S.L., Jagodnik, K.M., Lachmann, A., et al. (2016). Enrichr: a comprehensive gene set enrichment analysis web server 2016 update. Nucleic Acids Res. *44*, W90–W97. https://doi.org/10.1093/nar/gkw377.

Lay, K., Yuan, S., Gur-Cohen, S., Miao, Y., Han, T., Naik, S., Pasolli, H.A., Larsen, S.B., and Fuchs, E. (2018). Stem cells repurpose proliferation to contain a breach in their niche barrier. Elife *7*, e41661. https://doi.org/10.7554/eLife.41661.

Lee, J.-H., Bhang, D.H., Beede, A., Huang, T.L., Stripp, B.R., Bloch, K.D., Wagers, A.J., Tseng, Y.-H., Ryeom, S., and Kim, C.F. (2014). Lung stem cell differentiation in mice directed by endothelial cells via a BMP4-NFATc1-thrombospondin-1 axis. Cell *156*, 440–455. https://doi.org/10.1016/j.cell.2013.12.039.

Lutz, D., Gazdhar, A., Lopez-Rodriguez, E., Ruppert, C., Mahavadi, P., Günther, A., Klepetko, W., Bates, J.H., Smith, B., Geiser, T., et al. (2015). Alveolar derecruitment and collapse induration as crucial mechanisms in lung injury and fibrosis. Am. J. Respir. Cell Mol. Biol. *52*, 232–243. https://doi.org/10.1165/rcmb.2014-0078OC.

Madisen, L., Zwingman, T.A., Sunkin, S.M., Oh, S.W., Zariwala, H.A., Gu, H., Ng, L.L., Palmiter, R.D., Hawrylycz, M.J., Jones, A.R., et al. (2010). A robust and high-throughput Cre reporting and characterization system for the whole mouse brain. Nat. Neurosci. *13*, 133–140. https://doi.org/10.1038/nn.2467.

Mercer, R.R., Russell, M.L., and Crapo, J.D. (1994). Alveolar septal structure in different species. J. Appl. Physiol. *77*, 1060–1066. https://doi.org/10.1152/jappl.1994.77.3.1060.

Nabhan, A.N., Brownfield, D.G., Harbury, P.B., Krasnow, M.A., and Desai, T.J. (2018). Single-cell Wnt signaling niches maintain stemness of alveolar type 2 cells. Science *359*, 1118–1123. https://doi.org/10.1126/science.aam6603.

Nagendran, M., Riordan, D.P., Harbury, P.B., and Desai, T.J. (2018). Automated cell-type classification in intact tissues by single-cell molecular profiling. Elife *7*, e30510. https://doi.org/10.7554/eLife.30510.

Nikolić, M.Z., Sun, D., and Rawlins, E.L. (2018). Human lung development: recent progress and new challenges. Development *145*, dev163485. https://doi.org/10.1242/dev.163485.

Ochs, M., Nyengaard, J.R., Jung, A., Knudsen, L., Voigt, M., Wahlers, T., Richter, J., and Gundersen, H.J.G. (2004). The number of alveoli in the human lung. Am. J. Respir. Crit. Care Med. *169*, 120–124. https://doi.org/10.1164/rccm.200308-1107OC.

Pardo-Saganta, A., Tata, P.R., Law, B.M., Saez, B., Chow, R.D.-W., Prabhu, M., Gridley, T., and Rajagopal, J. (2015). Parent stem cells can serve as niches for their daughter cells. Nature *523*, 597–601. https://doi.org/10.1038/nature14553.

Pozarska, A., Rodríguez-Castillo, J.A., Surate Solaligue, D.E., Ntokou, A., Rath, P., Mižíková, I., Madurga, A., Mayer, K., Vadász, I., Herold, S., et al. (2017). Stereological monitoring of mouse lung alveolarization from the early postnatal period to adulthood. Am. J. Physiol. Lung Cell Mol. Physiol. *312*, L882–L895. https://doi.org/10.1152/ajplung.00492.2016.

Raina, D., Kosugi, M., Ahmad, R., Panchamoorthy, G., Rajabi, H., Alam, M., Shimamura, T., Shapiro, G.I., Supko, J., Kharbanda, S., and Kufe, D. (2011). Dependence on the MUC1-C oncoprotein in non-small cell lung cancer cells. Mol. Cancer Ther. *10*, 806–816. https://doi.org/10.1158/1535-7163.MCT-10-1050.

Rinkevich, Y., Lindau, P., Ueno, H., Longaker, M.T., and Weissman, I.L. (2011). Germ-layer and lineage-restricted stem/progenitors regenerate the mouse digit tip. Nature *476*, 409–413. https://doi.org/10.1038/nature10346.

Rock, J.R., Barkauskas, C.E., Cronce, M.J., Xue, Y., Harris, J.R., Liang, J., Noble, P.W., and Hogan, B.L.M. (2011). Multiple stromal populations contribute to pulmonary fibrosis without evidence for epithelial to mesenchymal transition. Proc. Natl. Acad. Sci. USA *108*, E1475–E1483. https://doi.org/10.1073/pnas.1117988108.

Rock, J.R., and Hogan, B.L.M. (2011). Epithelial progenitor cells in lung development, maintenance, repair, and disease. Annu. Rev. Cell Dev. Biol. *27*, 493–512. https://doi.org/10.1146/annurev-cellbio-100109-104040.

Rock, J.R., Randell, S.H., and Hogan, B.L.M. (2010). Airway basal stem cells: a perspective on their roles in epithelial homeostasis and remodeling. Dis. Model. Mech. *3*, 545–556. https://doi.org/10.1242/dmm.006031.

Rompolas, P., Mesa, K.R., and Greco, V. (2013). Spatial organization within a niche as a determinant of stem-cell fate. Nature *502*, 513–518. https://doi.org/10.1038/nature12602.

Rompolas, P., Mesa, K.R., Kawaguchi, K., Park, S., Gonzalez, D., Brown, S., Boucher, J., Klein, A.M., and Greco, V. (2016). Spatiotemporal coordination of stem cell commitment during epidermal homeostasis. Science *352*, 1471–1474. https://doi.org/10.1126/science.aaf7012.

Saito, M., Iwawaki, T., Taya, C., Yonekawa, H., Noda, M., Inui, Y., Mekada, E., Kimata, Y., Tsuru, A., and Kohno, K. (2001). Diphtheria toxin receptor-mediated conditional and targeted cell ablation in transgenic mice. Nat. Biotechnol. *19*, 746–750. https://doi.org/10.1038/90795.

Saltos, A., Khalil, F., Smith, M., Li, J., Schell, M., Antonia, S.J., and Gray, J.E. (2018). Clinical associations of mucin 1 in human lung cancer and precancerous lesions. Oncotarget *9*, 35666–35675. https://doi.org/10.18632/oncotarget.26278.

Schulte, H., Mühlfeld, C., and Brandenberger, C. (2019). Age-related structural and functional changes in the mouse lung. Front. Physiol. *10*, 1466. https://doi.org/10.3389/fphys.2019.01466.

Strunz, M., Simon, L.M., Ansari, M., Kathiriya, J.J., Angelidis, I., Mayr, C.H., Tsidiridis, G., Lange, M., Mattner, L.F., Yee, M., et al. (2020). Alveolar regeneration through a Krt8+ transitional stem cell state that persists in human lung fibrosis. Nat. Commun. *11*, 3559. https://doi.org/10.1038/s41467-020-17358-3.

Stuart, T., Butler, A., Hoffman, P., Hafemeister, C., Papalexi, E., Mauck, W.M., Hao, Y., Stoeckius, M., Smibert, P., and Satija, R. (2019). Comprehensive integration of single-cell data. Cell *177*, 1888–1902.e21. https://doi.org/10.1016/j.cell.2019.05.031.

Tata, P.R., Mou, H., Pardo-Saganta, A., Zhao, R., Prabhu, M., Law, B.M., Vinarsky, V., Cho, J.L., Breton, S., Sahay, A., et al. (2013). Dedifferentiation of committed epithelial cells into stem cells in vivo. Nature *503*, 218–223. https://doi.org/10.1038/nature12777.

Tata, P.R., and Rajagopal, J. (2016). Regulatory circuits and Bi-directional signaling between stem cells and their progeny. Cell Stem Cell *19*, 686–689. https://doi.org/10.1016/j.stem.2016.11.009.

Tuveson, D.A., Shaw, A.T., Willis, N.A., Silver, D.P., Jackson, E.L., Chang, S., Mercer, K.L., Grochow, R., Hock, H., Crowley, D., et al. (2004). Endogenous oncogenic K-ras(G12D) stimulates proliferation and widespread neoplastic

and developmental defects. Cancer Cell 5, 375–387.

van Amerongen, R., Bowman, A.N., and Nusse, R. (2012). Developmental stage and time dictate the fate of Wnt/β-catenin-responsive stem cells in the mammary gland. Cell Stem Cell 11, 387–400. https://doi.org/10.1016/j.stem.2012.05.023.

Warburton, D., Schwarz, M., Tefft, D., Flores-Delgado, G., Anderson, K.D., and Cardoso, W.V. (2000). The molecular basis of lung morphogenesis. Mech. Dev. 92, 55–81.

Weibel, E.R. (2015). On the tricks alveolar epithelial cells play to make a good lung. Am. J. Respir. Crit. Care Med. 191, 504–513. https://doi.org/10.1164/rccm.201409-1663OE.

Weibel, E.R. (1971). The mystery of "non-nucleated plates" in the alveolar epithelium of the lung explained. Acta Anat. 78, 425–443. https://doi.org/10.1159/000143605.

Weibel, E.R., and Gomez, D.M. (1962). Architecture of the human lung. Use of quantitative methods establishes fundamental relations between size and number of lung structures. Science 137, 577–585.

Weibel, E.R., Sapoval, B., and Filoche, M. (2005). Design of peripheral airways for efficient gas exchange. Respir. Physiol. Neurobiol. 148, 3–21. https://doi.org/10.1016/j.resp.2005.03.005.

Wilson, R.H., Meador, R.S., Jay, B.E., and Higgins, E. (1960). The pulmonary pathologic physiology of persons who smoke cigarettes. N. Engl. J. Med. 262, 956–961. https://doi.org/10.1056/NEJM196005122621903.

Xin, T., Greco, V., and Myung, P. (2016). Hardwiring stem cell communication through tissue structure. Cell 164, 1212–1225. https://doi.org/10.1016/j.cell.2016.02.041.

Young, M.D., and Behjati, S. (2020). SoupX removes ambient RNA contamination from droplet-based single-cell RNA sequencing data. GigaScience 9, giaa151. https://doi.org/10.1093/gigascience/giaa151.

Zacharias, W.J., Frank, D.B., Zepp, J.A., Morley, M.P., Alkhaleel, F.A., Kong, J., Zhou, S., Cantu, E., and Morrisey, E.E. (2018). Regeneration of the lung alveolus by an evolutionarily conserved epithelial progenitor. Nature 555, 251–255. https://doi.org/10.1038/nature25786.

Zepp, J.A., Morley, M.P., Loebel, C., Kremp, M.M., Chaudhry, F.N., Basil, M.C., Leach, J.P., Liberti, D.C., Niethamer, T.K., Ying, Y., et al. (2021). Genomic, epigenomic, and biophysical cues controlling the emergence of the lung alveolus. Science 371, eabc3172. https://doi.org/10.1126/science.abc3172.

Zepp, J.A., and Morrisey, E.E. (2019). Cellular crosstalk in the development and regeneration of the respiratory system. Nat. Rev. Mol. Cell Biol. 20, 551–566. https://doi.org/10.1038/s41580-019-0141-3.

# STAR★METHODS

## KEY RESOURCES TABLE

| REAGENT or RESOURCE | SOURCE | IDENTIFIER |
| --- | --- | --- |
| **Antibodies** | | |
| Rabbit Polyclonal anti-Prosurfactant protein C | Millipore | Cat# ab3786; RRID:AB_91588 |
| Monoclonal Rat anti-RAGE/AGER | R&D systems | Cat# MAB1179; RRID:AB_2289349 |
| Polyclonal Goat Human RAGE/AGER | R&D systems | Cat# AF1145; RRID:AB_354628 |
| Polyclonal Goat tdTomato | Origene | Cat# AB8181-200; RRID: AB_2722750 |
| Monoclonal American Hamster anti-MUC1 | ThermoFisher Scientific | Cat# MA5-11202; RRID: AB_11000874 |
| Polyclonal Rabbit Anti-Ezrin | Millipore | Cat# 07-130; RRID:AB_310383 |
| Monoclonal Mouse Anti-EPS8 | BD Biosciences | Cat# 610143; RRID:AB_397544 |
| Monoclonal Rat Anti-CD31 | BD Biosciences | Cat# 550274; RRID:AB_393571 |
| Polyclonal Guinea Pig anti-LAMP3 | Synaptic Systems | Cat# 391 005; RRID:AB_2713987 |
| Polyclonal Rabbit Anti-NKX2-1 | Santa Cruz Biotechnology | Cat# sc-13040; RRID:AB_793532 |
| Polyclonal Rabbit Anti-14-3-3 sigma | Thermo Fisher Scientific | Cat# PA5-95056; RRID:AB_2806862 |
| Monoclonal Rat Anti-B1-integrin | Abcam | Cat# ab25254; RRID:AB_2129042 |
| Monoclonal Rat Anti-E-cadherin | Thermo Fisher Scientific | Cat# 13-1900; RRID:AB_2533005 |
| Monoclonal Rat anit-mKi67 | Thermo Fisher Scientific | Cat# 14-5698-82; RRID: AB_10854564 |
| Monoclonal Rat anti-PECAM | BD Pharmingen | Cat# 550274; RRID: AB_393571 |
| LEL-Fluorescein | Vector Laboratories | Cat# FL-1171; RRID:AB_2307440 |
| Rabbit anti-SPRR1A | Kind gift from Dr. Stephen Strittmatter, Yale University | N/A |
| Alexa Fluor 594 goat anti-rabbit IgG | Thermo Fisher Scientific | Cat# A21207; RRID:AB_141637 |
| Alexa Fluor 594 donkey anti-goat IgG | Thermo Fisher Scientific | Cat# A11058; RRID:AB_2534105 |
| Alexa Fluor 647 goat anti-rat IgG | Thermo Fisher Scientific | Cat# A21247; RRID:AB_141778 |
| Alexa Fluor 647 goat anti-rabbit IgG | Thermo Fisher Scientific | Cat# A21245; RRID:AB_2535813 |
| Alexa Fluor 488 donkey anti-chicken IgG | Jackson Immuno | Cat# 703-545-155; RRID:AB_2340375 |
| Alexa Fluor 488 donkey anti-goat IgG | ThermoFisher | Cat# A11055; RRID:AB_2534102 |
| Alexa Fluor 647 donkey anti-guinea pig IgG | Jackson Immuno | Cat#706-605-148; RRID:AB_2340476 |
| CD45 microbeads, mouse | Miltenyi Biotec | Cat# 130-052-301; RRID:AB_2877061 |

*(Continued on next page)*

*Continued*

| REAGENT or RESOURCE | SOURCE | IDENTIFIER |
|---|---|---|
| Anti-CD31 microbeads | Miltenyi Biotec | Cat# 130-097-418; RRID:AB_2814657 |
| Anti-CD140a microbeads | Miltenyi Biotec | Cat# 130-101-547 |
| **Bacterial and virus strains** | | |
| NEB Stable Competent *E. coli* | NEB | Cat# C3040 |
| Adeno-Cre-GFP | Signagen | Cat# SL100706 |
| **Biological samples** | | |
| Human lung tissue | The University of North Carolina at Chapel Hill | N/A |
| **Chemicals, peptides, and recombinant proteins** | | |
| DMEM | Corning | Cat# 25-500 |
| Antibiotic-Antimycotic (100X) | Thermo Fisher Scientific | Cat# A5955-100ML |
| Penicillin/Streptomycin | Gibco | Cat# 15140 |
| FBS | HyClone products (Cytiva) | Cat# SH30396.03 |
| Tamoxifen | Sigma-Aldrich | Cat# T5648 |
| *Dispase* | Corning | Cat# 354235 |
| *DNase I* | Thermo Fisher Scientific | Cat# 10104159001 |
| *Collagenase type I* | Gibco | Cat# 17100-017 |
| TruStain FcX | Biolegend | Cat# 422302 |
| Diphtheria toxin | Millipore | Cat# 322326 |
| EdU | Life Technologies | Cat# EdU |
| Sucrose | Sigma-Aldrich | Cat# S9378 |
| Citrate Buffer, pH 6.0 (10X) | Sigma-Aldrich | Cat# C9999 |
| DAPI | Sigma-Aldrich | Cat# D9542 |
| Fluoromount-G, with DAPI | Thermo Fisher Scientific | Cat# 00-4959 |
| PBS | Gibco | Cat# 20012027 |
| 2YT Broth Powder | VWR | Cat# 100220-034 |
| *Age1-HF* Restriction Enzyme | NEB | Cat# R3552 |
| *Not1-HF* Restriction Enzyme | NEB | Cat# R3189 |
| Q5 High-Fidelity DNA Polymerase | NEB | Cat# M0491 |
| pJET1.2 cloning vector | Thermo Fisher Scientific | Cat# K1231 |
| Physiologic Saline | Henry Schein | Cat# 002477 |
| OCT Compound | Fisher Scientific | Cat# 23-730-571 |
| Glutaraldehyde | Sigma-Aldrich | Cat# G5882 |
| Paraformaldehyde | Sigma-Aldrich | Cat# P6148 |
| Low melting agarose | Seaplaque | Cat# 50100 |
| Chromium Next GEM Single Cell 3′ Kits v3.1 | 10x Genomics | Cat# 1000269 |
| Sodium Trichloroacetate | Sigma-Aldrich | Cat# 190780 |
| Ethylenediaminetetraacetic acid disodium salt dihydrate (EDTA) | Sigma-Aldrich | Cat# E5134 |
| Tris pH 7.4 | Thermo Fisher Scientific | Cat# J60202.K2 |
| Heparin ammonium sulfate from porcine intestinal mucosa | Sigma-Aldrich | Cat# H6279 |
| T4 DNA Ligase | NEB | Cat# M0202 |
| RNaseOUT | ThermoFisher | Cat# 10777019 |

*Continued*

| REAGENT or RESOURCE | SOURCE | IDENTIFIER |
|---|---|---|
| NxGen® phi29 DNA Polymerase | ThermoFisher | Cat# 30221-2 |
| Grace Bio-Labs SecureSeal™ hybridization chambers | Sigma-Aldrich | Cat# GBL621505-20EA |
| Pierce™ 16% Formaldehyde (w/v), Methanol-free | ThermoFisher | Cat# 28908 |
| Bleomycin | United States Pharmacopeia (USP) | Cat# 1076308 |
| 3R4F Research Cigarettes | University of Kentucky Reference Cigarette | N/A |
| **Deposited data** | | |
| Single-cell RNA-seq data | This study | NCBI GEO: GSE173878 |
| **Experimental models: Cell lines** | | |
| HEK293T cells | ATCC | Cat# CRL-3216 |
| **Experimental models: Organisms/strains** | | |
| Sftpc^tm1(cre/ERT2)Blh | Jackson Laboratory | Cat# 028054 |
| C57Bl/6 | Jackson Laboratory | Cat# 000664 |
| AKR/J | Jackson Laboratory | Cat# 000648 |
| Rosa26R-CAG-lsl-tdTomato | Jackson Laboratory | Cat# 007914 |
| Rosa26R-lsl-Rainbow | Rinkevich et al., 2011 | N/A |
| Rosa26R-lsl-DTA | Jackson Laboratory | Cat# 006331 |
| Rosa26R-lsl-KrasG12D | Jackson Laboratory | Cat# 008179 |
| Ager^tm1(cre/ERT2)Blh | Jackson Laboratory | Cat# 032771 |
| Axin2^tm1(cre/ERT2)Rnu/J | Jackson Laboratory | Cat# 018867 |
| Rosa26R-lsl-DTR | Jackson Laboratory | Cat# 007900 |
| Sprague Dawley rat lungs | Kindly provided by Cagla Eroglu, Duke University | N/A |
| **Oligonucleotides** | | |
| DTR forward: 5'-ACCGGTATGAAGCTGCTGCC GTCGGT-3' | Integrated DNA Technologies | N/A |
| DTR Reverse: 5'-GGATCCGTGGGAATTAGTCA TGCCCAACT-3' | Integrated DNA Technologies | N/A |
| MmHR2X-Wnt5b-1833: cagggtcac agacactcatcTTATACGTCGAGTTG AAGAACAACCTG | Integrated DNA Technologies | N/A |
| mmHL2X-Wnt5b-1833: TCGTACGT CTAACTTACGTCGTTATGttccccaca ggactgtagat | Integrated DNA Technologies | N/A |
| mmHR2X-Wnt5b-902: tggcaaagcggtagccgtacTTATACG TCGAGTTGAAGAACAACCTG | Integrated DNA Technologies | N/A |
| mmHL2X-Wnt5b-902 TCGTACGTCTAACTTACGTCGT TATGtccacgttgtctccacagcc | Integrated DNA Technologies | N/A |
| mmHR2X-Wnt5b-1275 agggagcctgtggtctcattTTATACGT CGAGTTGAAGAACAACCTG | Integrated DNA Technologies | N/A |

*(Continued on next page)*

**Continued**

| REAGENT or RESOURCE | SOURCE | IDENTIFIER |
|---|---|---|
| mmHL2X-Wnt5b-1275 TCGTACGTCTAACTTACGTCGT TATGacgcaggcagtagtcaggac | Integrated DNA Technologies | N/A |
| Recombinant DNA | | |
| pAAV Self-Complementary GFP | UNC Vector Core | N/A |
| Software and algorithms | | |
| CellRanger v3.0.0 | 10x genomics | https://www.10xgenomics.com/ |
| Seurat R package v3.2.3 | Stuart et al., 2019 | https://satijalab.org/seurat/ |
| SoupX pipeline | Young, M.D., Behjati, S. 2020 | https://github.com/constantAmateur/SoupX |
| Enrichr | Kuleshov et al., 2016 | https://maayanlab.cloud/Enrichr/ |
| Imaris | Oxford instruments | https://imaris.oxinst.com/ |
| GraphPad Prism | Graph Pad | https://www.graphpad.com |
| FIJI | NIH | https://fiji.sc |

## RESOURCE AVAILABILITY

### Lead contact

Further information and requests for resources and reagents should be directed to and will be fulfilled by the lead contact, Purushothama Rao Tata, purushothamarao.tata@duke.edu.

### Materials availability

This study did not generate unique reagents.

### Data and code availability

- Single-cell RNA-seq data have been deposited at GEO and are publicly available as of the date of publication and accession numbers are listed in the key resources table.

- This paper does not report original code.

- Any additional information required to reanalyze the data reported in this paper is available from the lead contact upon request.

## EXPERIMENTAL MODEL AND SUBJECT DETAILS

### Animals

*Sftpc$^{tm1(cre/ERT2)Blh}$*(*Sftpc-CreER*) (stock number 028054, Jackson Laboratory (Rock et al., 2011)), *Rosa26R-CAG-lsl-tdTomato (Ai14)* (stock number 007914, Jackson Laboratory (Madisen et al., 2010), *Rosa26R-lsl-DTA* (stock number 006331, Jackson Laboratory (Ivanova et al., 2005), *Rosa26R-lsl-Rainbow* (Rinkevich et al., 2011), *Rosa26R-lsl-KrasG12D* (stock number 008179, Jackson Laboratory (Jackson et al., 2001), *Ager$^{tm1(cre/ERT2)Blh}$* (*Ager-CreER*) (stock number 032771, Jackson Laboratory (Chung et al., 2018), *Axin2$^{tm1(cre/ERT2)Rnu}$*/J (*Axin2-CreER*) (stock number 018867, Jackson Laboratory (van Amerongen et al., 2012) and *Rosa26R-lsl-DTR* (stock number 007900, Jackson Laboratory (Buch et al., 2005) mice were maintained on a C57BL/6 background. For all lineage tracing or loss of function experiments, 3–5 doses of tamoxifen (0.1 mg/g body weight) (Sigma Aldrich) was administered intraperitoneally. For bleomycin injury, mice were administered 2.5U/kg bleomycin intranasally under isoflurane anesthesia and monitored daily. AAV5-DTR was administered intranasally at a dose of 2.5e10 viral genomes/mouse under isoflurane anesthesia in 60μL total volume. Diphtheria toxin was administered at a dose of 1μg/mouse (AT2 ablation) or 3μg/mouse (AT1 ablation) via intraperitoneal administration. To induce tumors, we intra-nasally administered adeno-Cre virus (Signagen, SL100706) (DuPage et al., 2009). EdU (E10187, Life Technologies) was administered intraperitoneally at a dose of 50mg/kg. 8–10 weekold Sprague Dawley female rats (Charles River, 001) were used for collection of all rat tissue. Animal experiments were approved by the Duke University Institutional Animal Care and Use Committee in accordance with US National Institutes of Health guidelines.

### Human lung tissue

Excised sub-transplant-quality human lung tissues from donors without pre-existing chronic lung diseases were procured through the Marsico Lung Institute at the University of North Carolina at Chapel Hill under the University of North Carolina Biomedical Institutional Review Board-approved protocol (#03-1396). Informed consent was obtained from all participants where necessary.

## METHOD DETAILS

### Tissue preparation and sectioning

Lungs were inflated with 4% Paraformaldehyde (PFA) and incubated at 4°C for 4–6 hours. Lung lobes were separated, washed in PBS, and incubated overnight in 30% sucrose at 4°C. Lobes were subsequently incubated in 1:1 30% sucrose:OCT for 1 hour followed by embedding in OCT blocks and cryosectioning. For all 2D imaging, sections were collected at 8–10μm.

For thick sections, 100–150μm OCT sections were collected in PBS. Alternatively, lungs were inflated with 1–1.5mL low-melting point 2% agarose dissolved in PBS. Lungs were placed on ice until agarose solidified, followed by vibratome sectioning at 75–100μm. Sections were collected in PFA, fixed for 4 hours at 4°C and stored in PBS until further processing. Human lung tissue was washed 3–5 times in PBS before agarose inflation. Lungs were placed on ice until agarose solidified, followed by vibratome sectioning at 75–100μm. Sections were collected in PFA, fixed for 4 hours at 4°C and stored in PBS until further processing. Rat lungs were inflated with low-melting point 2% agarose dissolved in PBS. Lungs were placed on ice until agarose solidified, followed by vibratome sectioning at 75–100μm. Sections were collected in PFA, fixed for 4 hours at 4°C and stored in PBS until further processing.

### Immunofluorescence staining

OCT sections were brought to room temperature and washed in PBS. Antigen retrieval was performed in citrate buffer, pH 6.0 (Sigma-Aldrich) using a water bath (95°C for 10–12 minutes) or antigen retrieval system (Electron Microscopy Science). Sections were washed with 0.1% Triton in PBS (PBST), incubated in blocking buffer (1% BSA in 0.1% PBST) for 1 hour, and then stained with primary antibody for 2 hours at RT or overnight at 4°C. Following primary antibody incubation, tissues were washed three times in PBST followed by incubation with secondary antibody in blocking buffer for 1 hour. Sections were washed with PBST and coverslips were mounted with Fluor G reagent with DAPI. Primary antibodies were as follows: Prosurfactant protein C (Millipore, ab3786, 1:500), RAGE/AGER (R&D systems, MAB1179, 1:500), mKi67 (Thermo Fisher, 14-5698-82, 1:250), TdTomato (Origene, AB8181-200, 1:700), MUC1 (Thermo Fisher, MA5-11202, 1:250), EZRIN (Millipore, 07-130, 1:300), EPS8 (BD Biosciences, 610143, 1:200), PECAM-1 (BD Pharmingen, 550274, 1:250), LAMP3 (Synaptic Systems, 391 005, 1:300), NKX2-1 (Santa Cruz, sc13040, 1:250), SFN (Thermo Fisher, PA5-95056, 1:250), B1-integrin (Abcam, ab25254, 1:100), E-cadherin (Thermo Fisher, 13-1900, 1:1000), LEL Fluorescin (Vector Laboratories, FL-1171, 1:1000), SPRR1A (1:1000, kindly provided by Dr. Stephen Strittmatter, Yale University).

For thick sections, immunofluorescence staining was performed on floating sections with buffers as described above. Thick sections were stained in primary antibody for 24–48 hours at 4°C, washed 3x in PBST for 15 minutes and incubated with secondary antibody for 3 hours at RT, followed by three washes with PBST. Nuclei were stained with 100 ng/mL DAPI for 15 minutes. Sections were maintained in PBS until imaging on a glass-bottom dish (Matsunami Glass).

### Plasmid construction, AAV production

Self-complementary GFP vector was obtained from the UNC Vector Core. The GFP cassette was replaced with coding sequence for diphtheria toxin receptor (DTR). Briefly, GFP was removed by Age1 and Not1 digestion. DTR open reading frame was synthesized as a Geneblock with SGI-DNA, amplified with the following primers and subcloned into pJET1.2 (ThermoFisher Scientific, K1231), as per manufacturer's protocol: forward, 5′-ACCGGTATGAAGCTGCTGCCGTCGGT-3′; reverse, 5′-GGATCCGTGGGAATTAGTCATGCCCAACT-3′. Insert was digested with Age1/Not1 and ligated into cut vector.

HEK293 (UNC Vector Core) were maintained in Dulbecco's Modified Eagle's Medium (DMEM) supplemented with 10% fetal bovine serum (FBS), 100U/ml penicillin, 100 μg/ml streptomycin. Cells were maintained in 5% $CO_2$ at 37°C. Recombinant AAV vectors were generated using triple plasmid transfection

with the AAV Rep-Cap plasmid (pXR5), Adenoviral helper plasmid (pXX680), and the DTR transgene cassette, flanked by AAV2-based inverted terminal repeat (ITR) sequences. Viral vectors were harvested from media and purified via iodixanol density gradient ultracentrifugation followed by phosphate buffered saline (PBS) buffer exchange. Titers of purified virus preparations were determined by quantitative PCR using a Roche Lightcycler 480 (Roche Applied Sciences, Pleasanton, CA) with primers amplifying the AAV2 ITR regions (forward, 5′-AACATGCTACGCAGAGAGGGAGTGG-3′; reverse, 5′-CATGAGACAAGGAA CCCCTAGTGA TGGAG-3′) (IDT Technologies, Ames IA).

### Live imaging of explanted lungs

Lungs were dissected, inflated with 1–1.5mL of 2% low-melting agarose (Seaplaque, 50100) dissolved in PBS. Inflated lungs were placed on ice until agarose solidified. Whole lobes were stained with LEL Fluorescein (Vector Laboratories, FL-1171, 1:500) to visualize alveolar cups. Following media acclimation, whole lobes were imaged using an Olympus FVMPE-RS multiphoton laser scanning microscope with a 25x NA 1.05 water-immersion objective. The system has a Spectra Physics Insight X3, laser tunable from 680nm-1300nm and a fixed 1045nm laser. 880 nm excitation was used for LEL fluorescing imaging and 1045 nm laser was used to acquire tdTomato signal with a 2 μm z step-size. Images were acquired every 10 minutes for 3 hours.

### Electron microscopy of lung tissue

Samples from mice lungs (Beike et al., 2019) and healthy, unused donor lungs (Lutz et al., 2015; Ochs et al., 2004) were taken from previous studies. Fixation and processing were performed using 1.5% Glutaraldehyde, 1.5% Paraformaldehyde in 0.15 M HEPES buffer, embedded in epoxy resin (Epon) and cut in 60 nm thick ultrathin sections. Electron microscopic analyses were performed using a FEI Morgani 268 transmission electron microscope (FEI, Eindhoven, Netherlands).

### Mouse lung tissue dissociation and cell isolation

Lungs were inflated with an enzyme dissociation solution (450U/mL *Collagenase I* (Worthington, LS004197), 5U/mL *Dispase* (Corning, 354235), and 0.33U/mL *DNase I* (Roche, 10104159001), in DMEM) (Katsura et al., 2020; Kobayashi et al., 2020; Konishi et al., 2022). Separated lung lobes were minced and incubated in enzyme solution at 37°C for 25 minutes. Dissociation was quenched with equivalent volume 10% FBS/DMEM and strained through a 100 μm strainer. Cell pellet was resuspended in red blood cell lysis buffer (100 μm EDTA, 10 mM $KHCO_3$, 155 mM $NH_4Cl$) for 2 minutes, followed by quenching with 10% FBS/DMEM and filtration through a 40 μm strainer.

For FACS sorting, the cell pellet was resuspended in 2mL 2%FBS/DMEM with *DNase I*. Antibodies used for sorting include the following: EPCAM (BioLegend, 118233, 1:200), CD31 (ThermoFisher, 48-0311-82, 1:200), CD45 (ThermoFisher, 48-0451-82, 1:200). Sorting was performed either using a FACS Vantage SE or SONY SH800S.

### Single-cell sequencing via 10Xgenomics

Lung tissue was dissociated as described above. Following red blood cell lysis and cell filtration, the resulting cell pellet was resuspended in 500μL 2%FBS/DMEM and split into three fractions: CD45/31/140a, CD45, and bulk sample. For MACS, cells were incubated for 30 minutes with the following antibodies: CD45 (MiltenyiBiotech, 130-052-301), CD31 (MiltenyiBiotech, 130-097-418), and CD140a (MiltenyiBiotech, 130-101-547). MACS depletion was performed as per manufacturer protocol using LD columns (MiltenyiBiotech, 130-042-901). For scRNA-seq, AT2 ablated lung cell suspension was first enriched for epithelial cell populations. For this, we combined different cell populations from AT2 ablated mice as follows: 11,200 cells from CD31/CD45/CD140a-depleted cells, 3200 cells from CD45-depleted cells, and 1600 cells from bulk fractions and resuspended in PBS supplemented with 0.01% BSA. Control mice were depleted only for CD31/CD45.

For single-cell RNA-sequencing, cells were captured, and libraries prepared using Chromium Single Cell 3′ Reagent Kits v3.1 (10x Genomics). Libraries were sequenced using Hi-SeQX with 150 bp-paired end sequencing followed by trimming of reads to meet manufacturer required amplicon length. FASTQ files were processed using CellRanger v3.0.0 (10x Genomics) and mapped to the mm10 reference genome.

Cellranger outputs were loaded into R and analyzed using the Seurat R package (v3.2.3) (Stuart et al., 2019). Cells were filtered using the SoupX pipeline (Young and Behjati, 2020). Low quality and duplet cells were

removed prior tofurther analysis (nFeature_RNA >1000 & nFeature_RNA <8000 &percent.mt <25 & nCount_RNA < 62000). Further processing was performed as per recommended Seurat pipeline: log normalization, identification of highly variable features (n = 5000), regression and scaling, and principal component analysis. Principle components, for which significance was based on Jackstraw plots, were used for generating UMAP plots. Specific cell clusters were identified based on enrichment for *Sftpc*, *Sftpb*, *Lamp3*, *Ager*, *Hopx*, *Akap5*, *Epcam*, *Mki67*, and *Top2a*. Specific markers for each cluster were obtained using *FindAllMarkers*, which were then used for gene ontology analysis through webgestalt.org. For pathway enrichment analyses, scaled data in the Seurat object were extracted to calculate mean values of gene members of represented pathways. These values were used to generate UMAP expression plots of signaling pathways. Genes that have ≥ 2 log2 fold change were used as input for Enrichr (Kuleshov et al., 2016) query to get enriched signaling pathways (Kuleshov et al., 2016).

### Proximity ligation *in situ* hybridization (PLISH)

Fixed frozen mouse lung sections were brought to room-temperature and post-fixed with 4% formalde-hyde for 20 minutes, treated with 20 μg mL$^{-1}$ proteinase K for 9 minutes at 37°C and dehydrated with increasing concentrations of ethanol (Nagendran et al., 2018). Sections were incubated with gene-specific oligos (listed below) in hybridization buffer (1 M sodium trichloroacetate, 50 mM Tris pH 7.4, 5 mM EDTA and 0.2 mg mL$^{-1}$ heparin) for 2 hours at 37°C. Common-bridge and circle probes were added to the sections and incubated for 1 hours, followed by a T4 DNA ligase reaction for 2 h. Rolling-circle amplification was performed using phi29 polymerase (Lucigen, 30221) for 12 hours at 37°C. Fluorophore-conjugated detection probe was applied and incubated for 30 minutes at 37°C, followed by mounting in medium containing 4,6-diamidino-2-phenylindole (DAPI).

mmHR2X-Wnt5b-1833 cagggtcacagacactcatcTTATACGTCGAGTTGAAGAACAACCTG

mmHL2X-Wnt5b-1833 TCGTACGTCTAACTTACGTCGTTATGttccccacaggactgtagat

mmHR2X-Wnt5b-902 tggcaaagcggtagccgtacTTATACGTCGAGTTGAAGAACAACCTG

mmHL2X-Wnt5b-902 TCGTACGTCTAACTTACGTCGTTATGtccacgttgtctccacagcc

mmHR2X-Wnt5b-1275 agggagcctgtggtctcattTTATACGTCGAGTTGAAGAACAACCTG

mmHL2X-Wnt5b-1275 TCGTACGTCTAACTTACGTCGTTATGacgcaggcagtagtcaggac

### *In vivo* cigarette smoke (CS) exposure

AKR/J and C57BL/6J mice (male and female) were purchased from Jackson Laboratories (Bar Harbor, ME). Mice (3-month-old) were exposed to 3R4F Research Cigarettes (University of Kentucky Reference Cigarette) for up to 6 hours/day, 5 days/week, for 4 months (AKR/J) or 6 months (C57BL/6J) using a total body CS exposure chamber (Teague TE-10, Teague Enterprises). The concentration of CS was periodically measured for total particulate matter, and concentration was maintained at 100–140 mg/m$^3$.

### Statistical analysis

Sample size was not pre-determined. Data are presented as means with standard error (SEM). Statistical analysis was performed in Excel, Prism, and R. A two-tailed Student's t-test was used for all comparisons between two conditions. In cases with >2 conditions, one-way ANOVA followed by Dunnett's multiple comparison's test. For multiple groups, two-way ANOVA followed by Sidak's multiple comparison's test were performed.

### Image acquisition and processing

Images were captured on an Olympus FV3000 confocal microscope using 20X, 40X, and 30X objectives and visualized using 3D projection in ImageJ or Imaris software (Bitplane). All surface rendering was performed in Imaris. Rainbow mouse tissues were imaged immediately prior to fixation using a Leica DMi8 STED and confocal microscope and are presented as a z-projection over approximately 40 microns. Quantification of Ki67 or EdU+ AT2s, AT1 differentiation, and MLI was performed on 2-D sections. All quantification of MUC1 domains was performed on 3D images to ensure no overlap or loss of MUC1 domain detail. AT2s that were not captured in full thickness were excluded from MUC1 domain analysis.